

AperTO - Archivio Istituzionale Open Access dell'Università di Torino

A possible new UHP unit in the Western Alps as revealed by ancient Roman quern-stones from Costigliole Saluzzo, Italy

This is a pre print version of the following article:

Original Citation:

Availability:

This version is available <http://hdl.handle.net/2318/1565906> since 2019-04-08T16:13:22Z

Published version:

DOI:10.1127/ejm/2016/0028-2531

Terms of use:

Open Access

Anyone can freely access the full text of works made available as "Open Access". Works made available under a Creative Commons license can be used according to the terms and conditions of said license. Use of all other works requires consent of the right holder (author or publisher) if not exempted from copyright protection by the applicable law.

(Article begins on next page)

1 **Cover page**

2

3 **Title:** A new UHP unit in the Western Alps possibly revealed by ancient Roman quern-stones from
4 Costigliole Saluzzo, Italy

5

6 **Running title:** Ancient quern-stones might reveal a new UHP unit in the Alps

7

8

9 **Detailed plan of the article (i.e. hierarchy of headings and subheadings)**

10 1. Introduction

11 2. Methods

12 2.1 Micro-X-ray fluorescence (μ -XRF) maps

13 2.2 Micro-Raman spectroscopy

14 2.3 Mineral chemistry

15 2.4 YAG (Y-in-garnet) thermometry

16 2.5 Phase diagrams computation

17 3. Petrography and mineral chemistry

18 4. Phase equilibria and P-T evolution

19 4.1 Stability field of the chloritoid + glaucophane + garnet \pm talc assemblage: previous studies

20 4.2 Thermodynamic modelling of the chloritoid + glaucophane + garnet + talc stability field

21 4.3 P-T evolution

22 5. Discussion

23 5.1 Petrogenesis of the coesite-bearing chloritoid + garnet \pm glaucophane talcschists

24 5.1.1 *Mg-rich protoliths metamorphosed in a closed-system*

25 5.1.2 *Felsic or mafic protoliths metamorphosed in an open-system (i.e. metasomatic*
26 *protoliths)*

27 5.2 Possible evidence for a new UHP unit in the southern Dora-Maira Massif

28 References

29 Figure captions

30

31

32 **Corresponding author:**

33 Simona Ferrando

34 simona.ferrando@unito.it

35 Tel. +39/0116705106

36 Fax: +39/0116705128

37 **Title page**

38

39 **A new UHP unit in the Western Alps possibly revealed by ancient Roman quern-stones**
40 **from Costigliole Saluzzo, Italy**

41

42

43

44 Chiara Groppo^{1,2}, Simona Ferrando^{1*}, Daniele Castelli¹, Diego Elia³, Valeria Meirano³, Luca
45 Facchinetti³

46

47

48

49 ¹Department of Earth Sciences, Via Valperga Caluso 35, I-10128 Torino, Italy

50 ²IGG-CNR, Via Valperga Caluso 35, I-10128 Torino, Italy

51 ³Department of Historical Studies, Via S. Ottavio 20, I-10124 Torino, Italy

52 *simona.ferrando@unito.it

53

54 **Abstract**

55 Peculiar coesite + chloritoid + garnet ± glaucophane talcschists have been used to make at least six
56 quern-stones, unearthed in the ruins of a *villa rustica* belonging to the Roman imperial period and
57 located at Costigliole Saluzzo, Western Alps. The site of the *villa rustica* and the presence of coesite
58 relics suggest a possible provenience of these rocks from the ultra-high pressure (UHP) Brossasco-
59 Isasca Unit (BIU) of the southern Dora-Maira Massif. However, similar talcschists have never been
60 reported from this Unit.

61 Two samples of coesite-bearing, chloritoid + garnet ± glaucophane –talcschist collected from
62 two different specimens of quern-stones, have been petrologically investigated with the aim of
63 constraining their peak P-T conditions. The stability field of the coesite + garnet + talc + chloritoid +
64 glaucophane assemblage has been constrained using isochemical phase diagrams modelled in the
65 MnNCFMASHO system; prograde P-T conditions have been additionally constrained using the
66 yttrium-in-garnet (YAG) geothermometer. Thermodynamic modelling tightly constrains peak P-T
67 conditions at 480-510°C, 27-31 kbar.

68 The unusual Mg-rich composition of the talcschists suggest that they originated by Mg-
69 metasomatism of either a granodioritic protolith or a Fe-rich metapelitic protolith. A mechanism
70 similar to that constrained for the well-known pyrope-bearing whiteschists of the UHP BIU, i.e. influx
71 of antigorite-derived fluids along shear zones during subduction, can be therefore envisaged.

72 Although the field occurrence of these coesite + chloritoid + garnet ± glaucophane talcschists
73 is still unknown, the obtained results clearly show that these rocks cannot belong to the UHP BIU,
74 whose peak P-T conditions are at significantly higher T and P (730°C, 40-43 kbar). Therefore, this
75 finding opens the challenging hypothesis of the existence of a further, still unmapped, UHP Unit in
76 the Southern Dora-Maira Massif that also experienced UHP metamorphism and fluid influx from
77 underlying serpentinites during subduction. A detailed mapping and petrologic investigation of the
78 tectono-metamorphic units adjacent to the BIU is required, in order to further constrain the location
79 and the dimension of this new UHP unit in the framework of the southern Dora-Maira Massif.

80
81 **Key-words:** coesite + chloritoid + garnet + glaucophane talcschist; UHP metamorphism; Mg-
82 metasomatism; southern Dora-Maira Massif; thermodynamic modeling; micro-Raman spectroscopy

83 1. Introduction

84 The ruins of a wide *villa rustica* belonging to the Roman imperial period were unearthed at the
85 southern periphery of the modern village of Costigliole Saluzzo (Fig. 1) and are still under excavation
86 (Elia & Meirano 2012; Elia *et al.*, 2013). In its major phase, the main building reached an extent of
87 around 5000 square metres. The evidence recovered supports the identification of two different
88 sections in the *villa*, the *pars urbana*, with a residential function, and the *pars rustica*, destined to
89 stocking agricultural products and to housing the productive units. Many fragments of quern-stones,
90 pertaining to at least 6 specimens, were retrieved in the building, mainly from a wide room which
91 acted as a kitchen and a butlery as well (Fig. 1b). The majority of the artefacts were in use when the
92 villa was destroyed by a fire at the end of the III c. AD. The hand-mills, up to 34-39 cm in diameter
93 (Fig. 2a,b), belong to two different types: a simpler and more common one, and a second type
94 provided with a particular mechanism in order to obtain different qualities of refined cereals (Fig. 2c).
95 They were carved from at least two different lithologies: (i) a coesite-bearing (micro-Raman
96 identification), chloritoid + garnet ± glaucophane –talcschist (Fig. 2d-f), and (ii) a phengite + garnet +
97 chloritoid ± glaucophane schist, with glaucophane pseudomorphically replaced by fine-grained
98 aggregates of white mica + biotite + albite.

99 The location of the ancient quarry is still unknown. Costigliole Saluzzo is located at the mouth
100 of Varaita Valley, some 5 km east of the ultra-high pressure (UHP) Brossasco-Isasca Unit (BIU),
101 tectonically sandwiched between the high-pressure (HP) San Chiaffredo and Rocca Solei Units of the
102 southern Dora-Maira Massif (Compagnoni *et al.*, 2012; Castelli *et al.*, 2014, with refs.) (Fig. 1a). The
103 site of the *villa rustica*, then, clearly points to a provenience of these rocks from the southern Dora-
104 Maira Massif. The presence of coesite relics seems to constrain the area of provenience to the UHP
105 BIU. However, talcschists with a similar mineral assemblage have never been reported from this Unit.
106 Therefore, this finding opens two challenging hypotheses: (i) the occurrence of still unrecognized,
107 peculiar “whiteschist” within the BIU; (ii) the existence of a second, still unmapped, UHP unit in the
108 southern Dora-Maira Massif.

109 In order to solve this conundrum, two samples of coesite-bearing, chloritoid + garnet ±
110 glaucophane –talcschist collected from two different specimens of quern-stones, have been
111 petrologically investigated with the aim of constraining their peak P-T conditions. The stability field of
112 the coesite + garnet + talc + chloritoid + glaucophane assemblage has been constrained using
113 isochemical phase diagrams modelled in the MnNCFMASHO system. Prograde P-T conditions have
114 been additionally constrained using the yttrium-in-garnet (YAG) geothermometer. The genesis of
115 these talcschists is discussed, considering two different possibilities: (i) derivation from a Mg-rich
116 protolith metamorphosed in a closed system, or (ii) metasomatic product of a mafic or felsic (either
117 granodiorite or metapelite) protolith.

118 The obtained results clearly suggest the existence of an UHP unit, whose peak P-T conditions
119 lies inside the coesite stability field but at significantly lower temperature than those estimated for
120 the BIU. A detailed mapping and petrologic investigation of the tectono-metamorphic units adjacent
121 to the BIU is required, in order to further constrain the location and the dimension of this new UHP
122 unit in the framework of the southern Dora-Maira Massif.

123

124 2. Methods

125 2.1 Micro-X-ray fluorescence (μ-XRF) maps

126 The micro-XRF maps of the whole thin sections (Fig. 3) were acquired using a μ-XRF Eagle III-XPL
127 spectrometer equipped with an EDS Si(Li) detector and with an Edax Vision32 microanalytical system

128 (Department of Earth Sciences, University of Torino, Italy). The operating conditions were as follows:
129 100 ms counting time, 40 kV accelerating voltage and a probe current of 900 μ A. A spatial resolution
130 of about 65 μ m in both x and y directions was used. Quantitative modal percentages of each mineral
131 were obtained by processing the μ -XRF maps with the software program "Petromod" (Cossio *et al.*
132 2002).

133

134 **2.2 Micro-Raman spectroscopy**

135 Micro-Raman spectra and map were acquired using the integrated micro/macro-Raman LABRAM
136 HRVIS (Horiba Jobin Yvon Instruments) of the Interdepartmental Center "G. Scansetti" (Department
137 of Earth Sciences, University of Torino, Italy), equipped with a computer-controlled, automated X-Y
138 mapping stage. Excitation lines at 532 nm (solid-state Nd laser and 80 mW of emission power) were
139 used, with Edge filter and a grating of 600 grooves/mm. Calibration was performed using the 520.6
140 cm^{-1} Si band. Each spectrum was collected by three accumulations of 5 s and with a laser spot of 4
141 μ m. The map of 140 μ m x 45 μ m, with steps of 1 μ m and a laser spot of 4 μ m, was acquired on the
142 sample surface by one accumulations of 1 s each step.

143

144 **2.3 Mineral chemistry**

145 Minerals were analysed with a Cambridge Stereoscan 360 SEM equipped with an EDS Energy 200 and
146 a Pentafet detector (Oxford Instruments) at the Department of Earth Sciences, University of Torino.
147 The operating conditions were as follows: 50 s counting time and 15 kV accelerating voltage. SEM-
148 EDS quantitative data (spot size = 2 μ m) were acquired and processed using the Microanalysis Suite
149 Issue 12, INCA Suite version 4.01; natural mineral standards were used to calibrate the raw data; the
150 $\rho\phi Z$ correction (Pouchou & Pichoir, 1988) was applied. Absolute error is 1 σ for all calculated oxides.

151 A JEOL 8200 Superprobe (WDS) was used at the Department of Earth Sciences, University of
152 Milano (Italy). Acceleration voltage was set to 15 kV, beam current was 15 nA and natural minerals
153 were used as standards. A $\rho\phi Z$ routine was used for matrix correction.

154 Mineral chemical data of representative minerals are reported in Fig.5, 6 and in Tables 1-2.

155

156 **2.4 YAG (yttrium-in-garnet) thermometry**

157 Temperature conditions for the growth of garnet core have been constrained by applying the
158 yttrium-in-garnet thermometry (YAG) of Pyle & Spear (2000). This empirical geothermometer
159 correlates the yttrium content in garnet with its temperature of formation, and is particularly
160 suitable for xenotime-bearing metapelites that experienced metamorphic temperature in the range
161 450-550 $^{\circ}$ C; errors estimated in this temperature interval are, in fact, of few degrees.

162

163 **2.5 Phase diagrams computation**

164 Isochemical phase diagrams were calculated in the MnNCFMASHO system using Perple_X (version
165 6.7.2, Connolly 1990, 2009) and the thermodynamic dataset and equation of state for H₂O-CO₂ fluid
166 of Holland & Powell (2011). The following solid solution models were used: garnet (White *et al.*,
167 2005), talc (ideal), chloritoid (Smye *et al.*, 2000), carpholite (Smye *et al.*, 2000), staurolite (ideal),
168 chlorite (Holland *et al.*, 1998), Na-amphibole (Dale *et al.*, 2000), plagioclase (Newton *et al.*, 1980),
169 omphacite (Diener & Powell, 2011) and epidote (Holland & Powell, 1998). Kyanite, quartz/coesite,
170 lawsonite, paragonite, magnetite and hematite were considered as pure end-members.

171 The bulk rock compositions of the studied samples have been calculated by combining the
172 mineral proportions obtained from the modal estimate of micro-XRF maps (Fig. 3) with mineral

173 chemistry acquired at SEM–EDS and WDS, and are reported in Table 3: these whole rock
174 compositions have been used to model the growth of garnet core, in equilibrium with chloritoid and
175 glaucophane cores. The possible effects of chemical fractionation of the bulk composition due to the
176 growth of the strongly zoned garnet porphyroblasts have been also considered. The bulk
177 compositions effectively in equilibrium during the growth of garnet rim have been therefore
178 calculated by subtracting the garnet core and mantle compositions to the whole rock compositions
179 (Table 3).

180

181 **3. Petrography, mineral chemistry and Raman spectroscopy**

182 The coesite-bearing chloritoid + garnet + glaucophane -talcschists (samples US900 and US773)
183 consist of quartz/coesite, talc, garnet, chloritoid, glaucophane, late Mg-chlorite (Fig.3, 4), abundant
184 accessory rutile, apatite and pyrite and minor xenotime (both in the matrix and in garnet). Mineral
185 assemblages and compositions are similar in both the samples, but mineral modes are quite
186 different. Sample US900 is quartz/coesite-, talc- and glaucophane -richer (vol%: Qz 38, Tlc 30, Cld 14,
187 Gln 9, Grt 8; mineral abbreviation after Whitney & Evans, 2010) than sample US773. Sample US773 is
188 chloritoid-richer than sample US900 and contains abundant Mg-chlorite, derived from chloritoid
189 retrogression (vol%: Qz 21, Tlc 22, Cld 23, Mg-Chl 23, Gln 3, Grt 8) (Fig. 3 and Table 3). Although rich
190 in talc, these rocks do not show a pervasive schistosity, due to the presence of garnet, chloritoid and
191 glaucophane porphyroblasts up to few millimetre in size, which partially obliterate the oriented
192 structure.

193 Chloritoid occurs as bluish-green, slightly zoned, porphyroblasts, with a darker core and a
194 lighter rim (Fig. 4f). It is locally pervasively replaced by a greenish Mg-chlorite, especially in sample
195 US773. Its X_{Mg} ranges from 0.29 in the core to 0.38 in the rim, whereas $X_{Fe^{+3}}$ is slightly higher in the
196 core than in the rim (core: $X_{Fe^{+3}} = 0.05-0.08$; rim: $X_{Fe^{+3}} = 0.04-0.07$) (Fig. 5d and Table 2)
197 [$X_{Mg}=Mg/(Mg+Fe)$; $X_{Fe^{+3}}=Fe^{+3}/(Fe^{+3}+Al)$].

198 Garnet porphyroblasts are idioblastic and strongly zoned (Fig. 4a-d), with a reddish core
199 ($X_{Fe}=0.73-0.79$, $X_{Mg}=0.07-0.09$, $X_{Mn}=0.05-0.12$, $X_{Ca}=0.08-0.10$), a pink mantle ($X_{Fe}=0.79-0.83$, $X_{Mg}=0.09-$
200 0.12 , $X_{Mn}=0.01-0.04$, $X_{Ca}=0.05-0.08$) and a colourless rim ($X_{Fe}=0.76-0.79$, $X_{Mg}=0.13-0.29$, $X_{Mn}=0.00-$
201 0.01 , $X_{Ca}=0.04-0.06$) (Table 1, Fig. 6a and Fig. S1, freely available online as Supplementary Material
202 linked to this article on the GSW website of the journal, <http://eurjmin.geoscienceworld.org/>). The
203 bell-shaped profile of Mn suggests a prograde garnet growth (Fig. 6b). Similarly to Mn, Y, Cr and Na
204 contents also show a bell-shaped profile (Fig. 6b). Maximum Y, Na and Cr contents in garnet core are
205 2000, 730, and 480 ppm, respectively, and decreases to almost zero in garnet rim. P has an opposite
206 trend: it is almost absent in garnet core and increases toward the rim, up to 220 ppm.

207 The garnet core and mantle includes chloritoid ($X_{Mg}=0.21-0.24$; $X_{Fe^{+3}}=0.07-0.10$) (Fig. 6d and
208 Fig. S1), very rare and fine-grained phengite (Si = 3.30 a.p.f.u. on the basis of 11 oxygens) locally
209 associated to chloritoid, and rare ilmenite (especially in the garnet core). The garnet mantle and rim
210 preserves relict coesite, partially inverted to quartz (Fig. 4c,d and Fig. S1). The garnet rim locally
211 includes talc, whereas fine-grained rutile is ubiquitous as inclusion in garnet.

212 Coesite inclusions preserved in garnet mantle are quite big (up to 200 μm) and poorly
213 retrogressed to quartz (Fig. 7a), compared to coesite included in garnet rim, that is mostly replaced
214 by quartz with a palisade structure (Fig. 7b) or by polycrystalline quartz (Fig. 7a). Garnet surrounding
215 the coesite inclusions shows the typical radial fractures due to the volume increase related to the
216 coesite-quartz inversion (Fig. 4c,d; Fig. 7b). The presence of coesite is confirmed by micro-Raman
217 analyses on exposed inclusions (Fig. 7c), which show the typical coesite vibrations (Frezzotti *et al.*,

218 2011). The upshift of most, but not all, of coesite peaks (e.g., the main peak at 523 cm⁻¹ instead of
219 521 cm⁻¹) indicates that a residual pressure is still preserved in the inclusions (e.g., Korsakov *et al.*,
220 2007; Khon, 2014). The best preserved, although exposed, single coesite inclusion has been selected
221 for Raman mapping (Fig. 7d). Also this coesite preserves a residual pressure (main peak at 524 cm⁻¹).
222 Quartz is optically detectable only in two cracks crosscutting the inclusion (Fig. 7d). Raman map (Fig.
223 7e) confirms the presence of quartz along the cracks, but also reveals the distribution of optically
224 undetectable quartz (i) as thin shell of 1-5 μm in thickness that completely surrounds the coesite
225 inclusion, and (ii) as thin veinlets (<5 μm in thickness) cutting the coesite. The main peak of quartz at
226 470 cm⁻¹ instead of 464 cm⁻¹ indicates an high residual pressure due to the coesite-to-quartz
227 transition (e.g., Korsakov *et al.*, 2009). These data confirm that the initial stage of inversion from
228 coesite to quartz subgrains occurs at grain boundaries between coesite and hosting garnet, and along
229 crosscutting cracks (e.g., Korsakov *et al.*, 2007).

230 A slightly-zoned, bluish to colourless glaucophane (abundant in sample US900: Fig. 3, 4a) is in
231 equilibrium with both chloritoid (Fig. 4e) and garnet rims and with talc. Its X_{Mg} and X_{Fe+3} are slightly
232 variable from core to rim (core: X_{Mg} = 0.70-0.74, X_{Fe+3} = 0.20-0.33; rim: X_{Mg} = 0.72-0.76, X_{Fe+3} = 0.14-
233 0.23) (Fig. 5a-c and Table 2). In the more retrograded sample US773, glaucophane is locally
234 surrounded by a thin and discontinuous rim of Na-Ca amphibole (winchite).

235 Talc has a X_{Mg}=0.85-0.88 (Table 2). Mg-chlorite is a late phase, developed at the expenses of
236 chloritoid in sample US7773 (Fig. 4b, f). Its composition is quite homogeneous, with a X_{Mg} = 0.60-0.71
237 (Table 2). Very rare epidote has also been observed in sample US773, and seems in equilibrium with
238 Mg-chlorite.

239

240 **4. Phase equilibria and P-T evolution**

241 **4.1 Stability field of the chloritoid + glaucophane + garnet ± talc assemblage: previous studies**

242 Chloritoid + glaucophane ± garnet and chloritoid + garnet + talc ± glaucophane assemblages are
243 typical of blueschists and low-T eclogites in high-pressure terranes around the world. The
244 coexistence of chloritoid + glaucophane ± garnet is reported in metapelitic rocks from the Variscan
245 Ile de Groix (Kienast & Triboulet, 1972; Bosse *et al.*, 2002), Vendée (Guiraud *et al.*, 1987) and Iberian
246 Massif (Lopez-Carmona *et al.*, 2010), the Gran Paradiso Massif of the western Alps (Chopin, 1981),
247 the Peloponnese in Greece (Katagas, 1980; Theye & Seidel, 1991), Turkey (Okay, 2002), Oman (El-
248 Shazly & Liou, 1991; Warren & Waters, 2006), New Caledonia (Ghent *et al.*, 1987), Sulawesi in
249 Indonesia (Miyazaki *et al.*, 1996), and the Chinese Tianshan (Wei *et al.*, 2009) and Qilian orogens (Wei
250 & Song, 2008).

251 Talc + chloritoid ± garnet ± glaucophane assemblages, similar to that observed in the studied
252 samples, are more rarely reported. They were described from the Gran Paradiso and Monte Rosa
253 Massifs of the western Alps (silvery micaschist: Compagnoni & Lombardo, 1974; Chopin, 1981;
254 Chopin & Moniè, 1984; Dal Piaz & Lombardo, 1986; Goffè & Chopin, 1986; Meffan-Main *et al.*, 2004;
255 Gabudianu Radulescu *et al.*, 2009), the Chinese Qilian orogen (Wei & Song, 2008) and the Tianshan of
256 Kazakhstan and Kyrgyzstan (Meyer *et al.*, 2014; Klemd *et al.*, 2015; Orozbaev *et al.*, 2015). This last
257 occurrence is worth of note, because of the presence of coesite relicts included in garnet.

258 Thermodynamic calculations in the model system NFMASH, NKFMAH and NCKFMASH (e.g.
259 Guiraud *et al.*, 1990; Proyer, 2003; Wei & Powell, 2004, 2006) suggested that the chloritoid +
260 glaucophane ± garnet assemblage is a high-pressure indicator in metapelites, being stable at
261 pressures higher than 18-19 kbar (except for Fe-rich compositions, where this assemblage is stable at
262 pressures as lower as 7-8 kbar: Wei & Song, 2008). The maximum stability field of the chloritoid +

263 glaucophane ± garnet assemblage is constrained at P = 19-35 kbar and T = 420-610 °C. In the quartz
264 stability field, this assemblage provides tight temperature constraints, being limited by the
265 appearance of the carpholite + jadeite assemblage at temperatures lower than ca. 420-430 °C and by
266 the appearance of garnet + kyanite + talc at temperature higher than ca. 600-610 °C. At pressures
267 above the quartz-coesite transition, the high-T boundary of this assemblage is still located at about
268 600 °C, whereas the low-T boundary is more P-dependent resulting in a field assemblage
269 progressively narrower toward high-P (Proyer, 2003; Wei & Powell, 2004, 2006). Furthermore,
270 chloritoid + glaucophane ± garnet assemblage is easily preserved during exhumation because it
271 requires external hydration in order to breakdown to lower pressures (Proyer, 2003).

272 The addition of talc results in a further limitation of the talc + chloritoid + glaucophane +
273 garnet stability field, limited at lower temperatures by the appearance of carpholite + chlorite/garnet
274 at about 530-550°C. This assemblage is predicted to be stable also at ultra-high pressure conditions,
275 in the narrow temperature range of about 550-600°C for P < 35 kbar (Proyer, 2003; Wei & Powell,
276 2004, 2006; Franz *et al.*, 2013).

277

278 **4.2 Thermodynamic modelling of the chloritoid + glaucophane + garnet + talc stability field**

279 The prograde P-T evolution of the less retrograded sample US900 has been constrained using two
280 different pseudosections calculated in the MnNCFMASHO model system, considering the
281 fractionation effects due to the growth of garnet porphyroblasts: (i) a first pseudosection, calculated
282 using the whole rock composition, has been used to model the growth of garnet core (Fig. 8a); (ii) a
283 second pseudosection, calculated using the effective bulk composition derived by subtracting garnet
284 cores and mantles to the whole rock composition, has been used to model the growth of garnet rim
285 (Fig. 8b).

286 The topologies of both pseudosections are very similar. The observed talc + chloritoid +
287 glaucophane + garnet assemblage is predicted to be stable in a quite small field. This field
288 assemblage is limited toward lower pressure and temperature by the presence of chlorite instead of
289 talc, toward higher pressure by the presence of carpholite instead of chloritoid and toward higher
290 temperature by the presence of kyanite instead of chloritoid (Fig. S2); furthermore, it extends up to
291 ca. 31 kbar, in the coesite-stability field (Fig. 8a,b). The dimension of the coesite + talc + chloritoid +
292 glaucophane + garnet field assemblage is mainly controlled by the carpholite-in and kyanite-in
293 trivariant reactions.

294 The position of the carpholite-in field boundary is critically dependent on the carpholite
295 thermodynamic parameters used in the calculation; it is worth of note that the topology of Fig. 8a,b
296 has been obtained using the most recent Holland & Powell (2011) database, whereas using older
297 versions of the same database, the coesite + talc + chloritoid + glaucophane + garnet field
298 assemblage is predicted to be stable in a narrower P-T field (Holland & Powell, 1998) or it is not
299 predicted to be stable at all (Holland & Powell, 1998, updated 2004; i.e. the talc + chloritoid +
300 glaucophane + garnet assemblage is only stable in the quartz stability field). The carpholite
301 thermodynamic parameters and, consequently, its stability field, have been a matter of debate in the
302 past (e.g. Vidal & Theye, 1996) and it is plausible that they are still not very well constrained.
303 However, the results obtained using the Holland & Powell (2011) database are in very good
304 agreement with the observed equilibrium assemblage and we are therefore confident that the
305 thermodynamic parameters of carpholite are now quite well calibrated.

306

307 **4.3 P-T evolution**

308 The pseudosection calculated using the whole rock bulk composition allowed to constrain the P-T
309 conditions for the growth of garnet core. Garnet core is predicted to grow in the quartz stability field,
310 at $T > 450$ °C, through chlorite breakdown (Fig. 8a). The modelled garnet and chloritoid
311 compositional isopleths [$X_{Mg}(Grt)=0.08$; $X_{Ca}(Grt)=0.09$; $X_{Mn}(Grt)=0.12$; $X_{Mg}(Cld)=0.29$] constrain the
312 growth of garnet core at ca. 450-480°C, 22-26 kbar, in the chlorite + glaucophane + garnet +
313 chloritoid + quartz + lawsonite field (lawsonite < 0.1 vol%; Fig. S2) (Fig. 8a). These temperature
314 conditions are in very good agreement with the results obtained using the YAG thermometer (Pyle &
315 Spear, 2000) applied on the maximum Y content measured in the garnet cores (i.e. 2000 ppm), which
316 gives a maximum temperature of 496 °C.

317 P-T conditions for the growth of garnet rim have been constrained using the pseudosection
318 calculated using the fractionated composition obtained by subtracting garnet cores and mantles to
319 the whole rock bulk composition. The main differences between the two pseudosections is the shift
320 of the garnet-in curve toward higher T and P for the fractionated pseudosection (Fig. 8b). The
321 modelled garnet and chloritoid compositional isopleths [$X_{Mg}(Grt)=0.20$; $X_{Ca}(Grt)=0.04$; $X_{Mn}(Grt)=0.00$;
322 $X_{Mg}(Cld)=0.37$] constrain the growth of garnet core at ca. 480-510°C, 25-31 kbar, in the talc +
323 chloritoid + glaucophane + garnet + quartz/coesite field. The occurrence of coesite still preserved in
324 garnet rim further constrain the P-T conditions of garnet rim at 480-510°C, 27-31 kbar (Fig. 8b).
325 Finally, the modelled isomodes predicts the following modal abundances at the estimated peak P-T
326 conditions: Coe36, Tlc29, Cld14, Gln12, Grt9 (vol%) (Fig. 8c-i), which are in very good agreement with
327 the observed modal proportions of the main mineral phases.

328 Overall, the P-T evolution resulting from the thermodynamic modelling and thermometric
329 results is characterized by a prograde increase in both pressure and temperature from ca. 460 °C, 25
330 kbar to ca. 510 °C, 28 kbar, just above the quartz to coesite transition (Fig. 9). The obtained results
331 also suggest the crucial role of the quartz-consuming reaction $Chl + Qz \rightarrow Cld + Grt + Tlc$ for the
332 formation of the observed equilibrium assemblage.

333 In sample US900, the retrogression effects are very scarce. The modelled H₂O isomodes show
334 that, during exhumation, the system was H₂O under-saturated whatever decompression path was
335 followed (either isobaric or cooling decompression) (Fig. 8l). This means that metamorphic reactions
336 could not proceed until H₂O-saturated conditions were again reached or, alternatively, H₂O was
337 introduced from outside (see Guiraud *et al.*, 2001 for the interpretation of H₂O-saturated vs. H₂O-
338 undersaturated conditions), and explains why the UHP assemblage remained preserved. On the
339 opposite, in sample US773, chlorite pervasively grew at the expenses of chloritoid, glaucophane is
340 locally rimmed by a discontinuous rim of NaCa-amphibole, and small epidote granoblasts
341 occasionally occur in the rock matrix. This incipient retrogression can only be justified by the addition
342 of a low H₂O amount from outside the system.

343

344 5. Discussion

345 5.1 Petrogenesis of the coesite-bearing chloritoid + garnet + glaucophane talcschists

346 The equilibrium assemblage observed in the studied rocks reflects a quite unusual Mg-rich
347 composition that requires further discussion as concerning the possible protolith and the genetic
348 processes involved in their formation. The studied talcschists can be described in a slightly oxidized
349 MgO-FeO-Al₂O₃-SiO₂-H₂O system with low amounts of Na₂O (< 1 wt%) and CaO (< 0.3 wt%) (Table 3).
350 They are not “whiteschist” *sensu stricto* because, according to the official nomenclature, they should
351 contain the assemblage talc + kyanite (or the UHP equivalent pyrope + kyanite) (Fettes & Desmons,
352 2007), whereas the term “silvery micaschist”, used for similar chloritoid ± garnet ± phengite

353 talcschists can be applied (e.g. Compagnoni & Lombardo, 1974; Meffan-Main *et al.*, 2004; Gabudianu
354 Radulescu *et al.*, 2009). Beside the high amount of MgO, they are characterized by significant
355 amounts of FeO_{tot} (up to 16 wt%) and are completely devoid of K₂O (Table 3).

356 Possible protoliths with a composition suitable to develop the observed equilibrium
357 assemblage are: (1) Mg-rich rocks of either sedimentary or volcanic nature, and (2) metasomatically
358 altered felsic or mafic rocks (see Franz *et al.*, 2013 for a discussion of the protoliths of whiteschists
359 and Ferrando, 2012 for a review on Mg-metasomatism of metagranitoids). The lack of field data and
360 of any information regarding the location of the ancient quarry from where these quern-stones were
361 extracted hampers a definitive interpretation of the protolith and of the genetic processes
362 responsible for the formation of the observed assemblage. However, because the site of the retrieval
363 of the quern-stones clearly points to a provenience of these rocks from the southern Dora-Maira
364 Massif, some speculations can be proposed.

365

366 **5.1.1 Mg-rich protoliths metamorphosed in a closed-system**

367 Franz *et al.* (2013) demonstrated that pre- or syn-metamorphic metasomatism is not an essential
368 prerequisite for the formation of Mg-rich and alkali-poor assemblages. Both weathered or
369 hydrothermally altered volcanic rocks and Mg-rich sedimentary protoliths can have a composition
370 suitable to develop talc-bearing assemblages. Among sedimentary protoliths, the best candidates are
371 palygorskite-rich clays deposited in continental lacustrine or in shallow marine environments, and
372 sepiolite, illite and/or smectite-rich pelitic rocks from evaporitic successions deposited in
373 epicontinental marine settings (see also Kulke & Schreyer, 1976; Schreyer, 1977; Moine *et al.*, 1981).

374 Although in principle a non-metasomatic origin cannot be excluded for the studied samples,
375 similar protoliths are unknown so far in the southern Dora-Maira Massif, which mainly consists of a
376 Variscan metamorphic basement (i.e. mainly amphibolite-facies metapelites with minor lenses of
377 metabasics and marbles) intruded by Permian granitoids.

378

379 **5.1.2 Felsic or mafic protoliths metamorphosed in an open-system (i.e. metasomatic protoliths)**

380 Although the chemical weathering could be locally responsible for the Mg-metasomatism of the
381 protolith of a HP-UHP rock (e.g., Franz *et al.*, 2013), in an orogenic setting such as the Alps many
382 other pervasive Mg-metasomatic processes widely occur and are more suitable to produce small
383 volumes (layers, lens-like bodies, veins, etc.) of Mg-metasomatic rocks. Ferrando (2012) discussed
384 the metasomatic processes responsible for the transformation of alkali-rich metagranitoids into Mg-
385 rich and alkali-poor metasomatic schists in the Alps, and demonstrated that these processes were
386 widespread and can be ascribed to different tectonic settings that were active at different times.
387 From this review, the most common Mg-metasomatic process that affected the continental crustal
388 rocks of the Alps along shear zones results to be the pervasive influx of Mg-rich, highly channelized
389 fluids derived from ultramafics previously interacting with seawater. This process can occur during
390 the rift-related ocean-continent transition, the continental subduction and/or the continent-
391 continent collision. The metasomatic products are typically characterized by strong depletions in
392 alkalis (very low or even null K₂O and Na₂O contents) and low depletions in silica, and by strong
393 enrichments in MgO (+ minor NiO₂ and/or Cr₂O₃) and by variable enrichments in FeO_{tot} depending on
394 the initial composition of the protolith. Mg-metasomatic rocks formed at the expenses of granitic
395 protoliths (e.g. the well-known pyrope-bearing whiteschists of the Brossasco-Isasca Unit; Ferrando *et al.*,
396 2009) are low in FeO_{tot} (< 2 wt%), whereas those formed at the expenses of granodioritic
397 protoliths are significantly richer in FeO_{tot}. For example, chlorite + garnet + staurolite schists (almost
398 free of quartz) with up to ca. 19 wt% of FeO_{tot}, but with low Na₂O (< 0.5 wt%) and SiO₂ (< 32 wt%)

399 and relatively high CaO (> 0.7 wt%) and K₂O (> 3.5 wt%), are described as the final metasomatic
400 product of a metagranodiorite from the Tauern window of eastern Alps (Selverstone *et al.*, 1991;
401 Barnes *et al.*, 2004).

402 Meyer *et al.* (2014) described coesite-bearing garnet + chloritoid talcschists with mineral
403 assemblage and compositions similar to those described in this study, but with a significantly lower
404 modal amount of quartz (< 5 vol%) and lacking of glaucophane. Because the field evidence shows
405 that the talcschists envelop blocks and boudins of mafic oceanic rocks tectonically embedded in
406 continentally derived metasediments, these Authors interpreted the talcschists as the metasomatic
407 product of a mafic protolith (either hydrothermally altered oceanic crust or volcanoclastic rock). Also
408 these talcschists are characterized by high FeO_{tot} contents (FeO_{tot} = 20 wt%) and very low alkalis, but
409 show a low SiO₂ content (45 wt%).

410 Both these two protoliths, i.e. granitoids and strongly altered mafic rocks, can be reasonably
411 excluded for the studied rocks. The studied talcschists cannot derive from a Fe-rich metagranitoid,
412 i.e. a metagranodiorite, because the amounts of Na₂O and SiO₂ are too high and those of CaO and
413 K₂O are too low compared with the previously documented examples of metasomatic granodiorites
414 (Selverstone *et al.*, 1991; Barnes *et al.*, 2004). Moreover, metagranodiorites, or chemically equivalent
415 orthogneisses, are not reported in the southern Dora-Maira Massif (e.g. Compagnoni *et al.*, 2012 and
416 references therein). Similarly, a protolith consisting of altered oceanic crust or altered volcanoclastic
417 rocks, is not compatible with the bulk of the studied rocks and is not coherent with the tectonic
418 setting of the southern Dora-Maira Massif (e.g. Compagnoni *et al.*, 2012).

419 One of the quern-stone associated to those carved from the talcschists is carved from a
420 garnet + chloritoid + glaucophane phengitic schist (Fig. S3), i.e. a widespread lithology outcropping in
421 the Rocca-Solei Unit (e.g. Compagnoni & Rolfo, 2003; Compagnoni *et al.*, 2012). Although we cannot
422 prove that this quern-stone was extracted from the same locality of the studied coesite + chloritoid +
423 garnet ± glaucophane talcschists, we can speculate that this lithology might represent the most
424 credible non-metasomatized equivalent of the talcschists. If it is the case, the Mg-metasomatism
425 could have moderately affected a “common” Fe-rich metapelite such as those that constitute the
426 majority of the Variscan basement in the southern Dora-Maira Massif.

427 Regarding the kind of metasomatism and its timing, the relatively high Cr content in garnet
428 points to the involvement of mantle derived fluids, and both microstructural relationships and
429 minerochemical data point to a process occurred before the garnet growth (i.e. at P < 25 kbar). In
430 fact, the Cr concentration decreases from garnet core to rim (Fig. 6b), opposite to what would be
431 expected if a Mg-rich, mantle derived, metasomatic fluid was introduced in the system after the
432 growth of garnet core (e.g. Ferrando *et al.*, 2009). This implies that the metasomatic process could
433 have occurred during early subduction, such as occurred for the well-known pyrope-bearing
434 whiteschists in the UHP Brossasco-Isasca Unit (Ferrando *et al.*, 2009), i.e. by a prograde influx of
435 antigorite-derived fluids along shear zones. However, as an alternative process, the metasomatism
436 could have occurred during the opening of the Tethyan basin, when fluids derived from hydrated
437 ultramafic rocks could have infiltrated the continental crust along rift-related detachment systems
438 (Ferrando, 2012).

439

440 **5.2 Possible evidence for a new UHP unit in the southern Dora-Maira Massif**

441 The location of the *villa rustica* and the occurrence of coesite relics, might have suggested the
442 obvious conclusion that the studied talcschists come from the nearby UHP Brossasco-Isasca Unit
443 (BIU), which is only ca. 5 km from Costigliole Saluzzo (Fig. 1a). However, the results of
444 thermodynamic modelling clearly show that the studied talcschists experienced peak P-T conditions

445 at UHP conditions, but at significant lower temperature (and pressure) than the BIU (Fig. 9). In the
446 western Alps, the only other UHP unit known so far is the Lago di Cignana Unit (e.g. Reinecke, 1991;
447 Groppo *et al.*, 2009; Frezzotti *et al.*, 2011), located in the Internal Piemontese Zone (Zermatt-Saas
448 Zone) of the upper Valtournanche, ca. 150 km from Costigliole Saluzzo. The calculated P-T conditions
449 for the prograde and peak stages do not match with the P-T path obtained for the Lago di Cignana
450 Unit (Groppo *et al.*, 2009) and it can be, therefore, excluded that the quern-stones come from there.

451 The high number of quern-stones carved from garnet + chloritoid + glaucophane talcschist
452 and phengitic schists unearthed in the *villa rustica* suggests that they were not realized starting from
453 a small outcrop or block occasionally found in the surroundings, but that a small quarry should have
454 existed, likely set in correspondence of a talcschist horizon (thick at least few meters and with a good
455 lateral continuity) possibly within the phengitic schists of the Rocca-Solei Unit. Coesite relics have
456 been never reported so far from this Unit; however, the Rocca-Solei Unit has been significantly less
457 studied than the BIU (the last petrological works date back to more than 15 years ago: Chopin *et al.*,
458 1991; Matsumoto & Hirajima, 2000) and it is possible that a systematic search for UHP evidence
459 could led to new coesite findings in the next future.

460 Further fieldwork and petrological investigation are therefore required in order to confirm
461 (or disprove) the existence of a second UHP unit in the southern Dora-Maira Massif. Such a discovery
462 could potentially have important implications for the understanding of the subduction and
463 exhumation processes that were active in convergent settings and that were responsible for the
464 actual architecture of the Alpine chain.

465

466 **Acknowledgements**

467 We gratefully acknowledge Roberto Compagnoni for being a constant source of inspiration and for
468 sharing his longstanding experience: we are indebted to him for most of our knowledge about the
469 southern Dora-Maira Massif.

470 Raman analytical facilities were provided by the Interdepartmental Center "G. Scansetti" and by the
471 Compagnia di San Paolo, Torino, Italy.

472 **References**

- 473 Barnes, J.D., Selverstone, J., Sharp, Z.D. (2004): Interactions between serpentinite devolatilization,
474 metasomatism and strike-slip strain localization during deep-crustal shearing in the Eastern Alps. *J.*
475 *Metamorph. Geol.*, **22**, 283–300.
- 476 Bosse, V., Balleuvre, M., Vidal, O. (2002): Ductile thrusting recorded by the garnet isograd from
477 blueschist-facies metapelites of the Ile de Groix, Armorican Massif, France. *J. Petrol.*, **43**, 485–510.
- 478 Castelli, D., Compagnoni, R., Lombardo, B., Angiboust, S., Balestro, G., Ferrando, S., Groppo, C.,
479 Hirajima, T., Rolfo, F. (2014): Crust-mantle interactions during subduction of oceanic & continental
480 crust. 10th International Eclogite Conference, Courmayeur (Aosta, Italy): Post-conference
481 excursions: September 9-10, 2013. *Geological Field Trips*, **6 (1.3)**, 73 pp.
- 482 Chopin, C., Henry, C., Michard, A. (1991): Geology and petrology of the coesite-bearing terrain, Dora
483 Maira massif, Western Alps. *Eur. J. Mineral.*, **3**, 263–291.
- 484 Chopin, C. & Monié, P. (1984): A unique magnesiochloritoid-bearing, high-pressure assemblage from
485 the Monte Rosa, Western Alps: petrologic and $^{40}\text{Ar}/^{39}\text{Ar}$ radiometric study. *Contrib. Mineral. Petrol.*,
486 **87**, 388–398.
- 487 Chopin, C. (1981): Talc-phengite: a widespread assemblage in high-grade pelitic blueschists of the
488 Western Alps. *J. Petrol.*, **22**, 628–650.
- 489 Compagnoni, R. & Rolfo, F. (2003): Ultrahigh-pressure units in the Western Alps. *in*: “Ultrahigh-
490 pressure metamorphism”, D.A. Carswell & R. Compagnoni, eds., EMU Notes in Mineralogy, 5, 13–
491 49.
- 492 Compagnoni, R., Rolfo, F., Groppo, C., Hirajima, T., Turello, R. (2012): Geologic map of the UHP
493 Brossasco-Isasca Unit (Western Alps). *J. Maps*, **8**, 465–472.
- 494 Compagnoni, R. & Lombardo, B. (1974): The Alpine age of the Gran Paradiso eclogites. *Rend. Soc. It.*
495 *Mineral. Petrol.*, **30**, 223–237.
- 496 Connolly, J.A.D. (2009): The geodynamic equation of state: what and how. *Geochem. Geophys.*
497 *Geosyst.*, **10**, Q10014.
- 498 Connolly, J.A.D. (1990): Multivariable phase diagrams: an algorithm based on generalized
499 thermodynamics. *Am. J. Sci.*, **290**, 666–718.
- 500 Cossio, R., Borghi, A., Ruffini, R. (2002): Quantitative modal determination of geological samples
501 based on X-ray multielemental map acquisition. *Microsc. Microanal.*, **8**, 139–149.
- 502 Dal Piaz, G. & Lombardo, B. (1986): Early Alpine eclogite metamorphism in the Penninic Monte Rosa-
503 Gran Paradiso basement nappes of the northwestern Alps. *Geol. Soc. Am. Bull.*, **164**, 249–265.
- 504 Dale, J., Holland, T., Powell, R. (2000): Hornblende-garnet-plagioclase thermobarometry: a natural
505 assemblage calibration of the thermodynamics of hornblende. *Contrib. Mineral. Petrol.*, **140**, 353–
506 362.
- 507 Diener, J.F.A. & Powell R. (2011): Revised activity–composition models for clinopyroxene and
508 amphibole. *J. Metamorph. Geol.*, **30**, 131–142.
- 509 Donner, M. & Marzoli, C. (1994): La macinazione. Evoluzione delle tecniche e degli strumenti. *In*: “Il
510 grano e le macine: la macinazione di cereali in Alto Adige, dall’Antichità al Medioevo”, S. de
511 Rachewiltz, L. Dal Ri, C. Marzoli, eds., Castel Tirolo, 73-93.
- 512 Elia, D. & Meirano, V. (2012): La villa di Costigliole Saluzzo (CN). Contributo alla conoscenza del
513 territorio piemontese in età romana. *Orizzonti. Rassegna di Archeologia*, **XIII**, 43–65.
- 514 Elia, D., Meirano, V., Russo, D. (2013): Costigliole Saluzzo, località Cimitero. Insediamento di età
515 romana. Interventi di scavo e di restauro: campagna 2012. *Quaderni della Soprintendenza*
516 *Archeologica del Piemonte*, **28**, 220–223.

517 El-Shazly, A.E.D.K. & Liou, J.G. (1991): Glaucofane-chloritoid-bearing assemblages from NE Oman:
518 petrologic significance and petrogenetic grid for high P metapelites. *Contrib. Mineral. Petrol.*, **107**,
519 180–201.

520 Ferrando, S. (2012): Mg-metasomatism of metagranitoids from the Alps: genesis and possible
521 tectonic scenarios. *Terra Nova*, **24**, 423 *Contrib. Mineral. Petrol.*, 436.

522 Ferrando, S., Frezzotti, M.L., Petrelli, M., Compagnoni, R. (2009): Metasomatism of continental crust
523 during subduction: the UHP whiteschists from the Southern Dora-Maira Massif (Italian Western
524 Alps). *J. Metamorph. Geol.*, **27**, 739–756.

525 Fettes, D. & Desmons, J. (2007): Metamorphic rocks. A Classification and Glossary of Terms.
526 Recommendations of the International Union of Geological Sciences Subcommittee on the
527 Systematics of Metamorphic Rocks. Cambridge University Press, Cambridge, 244 pp.

528 Franz, L., Romer, R.L., de Capitani, C. (2013): Protoliths and phase petrology of whiteschists. *Contrib.*
529 *Mineral. Petrol.*, **166**, 255–274.

530 Frezzotti, M.L., Selverstone, J., Sharp, Z.D., Compagnoni, R. (2011): Carbonate dissolution during
531 subduction revealed by diamond-bearing rocks from the Alps. *Nat. Geosci.*, **4**, 703–706.

532 Frezzotti, M.L., Tecce, F., Casagli, A. (2011): Raman spectroscopy for fluid inclusion analysis. *J.*
533 *Geochem. Explor.*, **112**, 1-20.

534 Gabudianu Radulescu, I., Rubatto, D., Gregory, C., Compagnoni, R. (2009): The age of HP
535 metamorphism in the Gran Paradiso Massif, Western Alps: a petrological and geochronological
536 study of “silvery micaschists”. *Lithos*, **110**, 95–108.

537 Ghent, E.D., Stout, M.Z., Black, P.M., Brothers, R.N. (1987): Chloritoid-bearing rocks associated with
538 blueschists and eclogites, northern New Caledonia. *J. Metamorph. Geol.*, **5**, 239–254.

539 Goffé, B. & Chopin, C. (1986): High-pressure metamorphism in the Western Alps: zoneography of
540 metapelites, chronology and consequences. *Schweiz. Mineral. Petrog. Mitt.*, **66**, 41–52.

541 Groppo, C., Beltrando, M., Compagnoni, R. (2009): P-T path of the UHP Lago di Cignana and adjoining
542 HP meta-ophiolitic units: insights into the evolution of subducting tethyan slab. *J. Metamorph.*
543 *Geol.*, **27**, 207–231.

544 Guiraud, M., Burg, J.P., Powell, R. (1987): Evidence for a Variscan suture zone in the Vendée, France:
545 a petrological study of blueschist facies rocks from Bois de Cene. *J. Metamorph. Geol.*, **5**, 225–237.

546 Guiraud, M., Holland, T., Powell, R. (1990): Calculated mineral equilibria in the greenschist-
547 blueschist-eclogite facies in Na₂O-FeO-MgO-Al₂O₃-SiO₂-H₂O. *Contrib. Mineral. Petrol.*, **104**, 85–98.

548 Guiraud, M., Powell, R., Rebay, G. (2001): H₂O in metamorphism and unexpected behaviour in the
549 preservation of metamorphic mineral assemblages. *J. Metamorph. Geol.*, **19**, 445–454.

550 Holland, T.J.B. & Powell, R. (2011): An improved and extended internally consistent thermodynamic
551 dataset for phases of petrological interest, involving a new equation of state for solids. *J.*
552 *Metamorph. Geol.*, **29**, 333–383.

553 Holland, J.T.B., Baker, J., Powell, R. (1998): Mixing properties and activity-composition relationships
554 of chlorites in the system MgO-FeO-Al₂O₃-SiO₂-H₂O. *Eur. J. Mineral.*, **10**, 395–406.

555 Katagas, C. (1980): Ferrograucofane and chloritoid-bearing metapelites from the phyllite series,
556 southern Peloponnese, Greece. *Mineral. Mag.*, **43**, 975–978.

557 Kiénast, J.R. & Triboulet, C. (1972): Le chloritoïde dans les paragenèses à glaucophane, albite ou
558 paragonite. *Bull. Soc. Franc. Minéral. Cristall.*, **95**, 565–573.

559 Klemd, R., Gao, J., Li, J.-L., Meyer, M. (2015): Metamorphic evolution of (ultra)-high-pressure
560 subduction-related transient crust in the South Tianshan Orogen (Central Asian Orogenic Belt):
561 Geodynamic implications. *Gondw. Res.*, **28**, 1–25.

562 Kohn, M.J. (2014): “Thermoba-Raman-try”: Calibration of spectroscopic barometers and
563 thermometers for mineral inclusions. *Earth Planet. Sci. Lett.*, **388**, 187-196.

564 Korsakov, A.V., Hutsebaut, D., Theunissen, K., Vandenabeele, P., Stepanov, A.S. (2007): Raman
565 mapping of coesite inclusions in garnet from the Kokchetav Massif (Northern Kazakhstan).
566 *Spectrochim. Acta Part A*, **68**, 1046-1052.

567 Korsakov, A.V., Perraki, M., Zhukov, V.P., De Gussem, K., Vandenabeele, P., Tomilenko, A.A. (2009): Is
568 quartz a potential indicator of ultrahigh-pressure metamorphism? Laser Raman spectroscopy of
569 quartz inclusions in ultrahigh-pressure garnets. *Eur. J. Mineral.*, **21**, 1313-1323.

570 Kulke, H. & Schreyer, W. (1973): Kyanite–talc–schist from Sar E Sang, Afghanistan. *Earth Planet. Sci.*
571 *Lett.*, **18**, 324–328.

572 Lopez-Carmona, A., Abati, J., Reche, J. (2010): Petrologic modeling of chloritoid–glaucophane schists
573 from the NW Iberian Massif. *Gondw. Res.*, **17**, 377–391.

574 Matsumoto, N. & Hirajima, T. (2000): Garnet in pelitic schists from a quartz-eclogite unit in the
575 southern Dora-Maira massif, Western Alps. *Schweiz. Mineral. Petrog. Mitt.*, **80**, 55–62.

576 Meffan-Main, S., Cliff, R.A., Barnicoat, A.C., Lombardo, B., Compagnoni, R. (2004): A tertiary age for
577 Alpine high pressure metamorphism in the Gran Paradiso massif, Western Alps: a Rb-Sr
578 microsampling study. *J. Metamorph. Geol.*, **22**, 267–281.

579 Meyer, M., Klemd, R., Hegner, E., Konopelko, D. (2014): Subduction and exhumation mechanisms of
580 ultra-high and high-P oceanic and continental crust at Makbal (Tianshan, Kazakhstan and
581 Kyrgyzstan). *J. Metamorph. Geol.*, **32**, 861–884.

582 Miyazaki, K., Zulkarnain, I., Sopaheluwakan, J., Wakita, K. (1996): Pressure-temperature conditions
583 and retrograde paths of eclogites, garnet-glaucophane rocks and schists from South Sulawesi,
584 Indonesia. *J. Metamorph. Geol.*, **14**, 549–563.

585 Moine, B., Sauvan, P., Jarousse, J. (1981): Geochemistry of evaporitic-bearing series: a tentative guide
586 for the identification of metaevaporites. *Contrib. Miner. Petrol.*, **76**, 401–412.

587 Newton, R.C., Charlu, T.V., Kleppa, O.J. (1980): Thermochemistry of the high structural state
588 plagioclases. *Geoch. Cosmoch. Acta*, **44**, 933–941.

589 Okay, A.I. (2002): Jadeite-chloritoid-glaucophane-lawsonite blueschists from north-west Turkey:
590 unusually high P/T ratios in continental crust. *J. Metamorph. Geol.*, **20**, 757–768.

591 Orozbaev, R., Hirajima, T., Bakirov, A., Takasu, A., Maki, K., Yoshida, K., Sakiev, K., Bakirov, A., Hirata,
592 T., Tagiri, M., Togonbaeva, A. (2015): Trace element characteristics of clinozoisite pseudomorphs
593 after lawsonite in talc-garnet-chloritoid schists from the Makbal UHP Complex, northern Kyrgyz
594 Tian-Shan. *Lithos*, **226**, 98–115.

595 Pouchou, J.L. & Pichoir, F. (1988): Determination of mass absorption coefficients for soft X-Rays by
596 use of the electron microprobe. *Microbeam Analysis*, San Francisco Press, pp 319–324.

597 Proyer, A. (2003): Metamorphism of pelites in NKFMAHSH - a new petrogenetic grid with implications
598 for the preservation of high pressure mineral assemblages during exhumation. *J. Metamorph.*
599 *Geol.*, **21**, 493–509.

600 Pyle, J.M. & Spear, F.S. (2000): An empirical garnet (YAG) ± xenotime thermometer. *Contrib. Mineral.*
601 *Petrol.*, **138**, 51–58.

602 Reinecke, T. (1991): Very-high pressure metamorphism and uplift of coesite-bearing metasediments
603 from the Zermatt-Saas zone, Western Alps. *Eur. J. Mineral.*, **3**, 7–17.

604 Schreyer, W. (1977): Whiteschists: their compositions and pressure–temperature regimes based on
605 experimental, field and petrographic evidence. *Tectonophysics*, **34**, 127–144.

606 Selverstone, J., Morteani, G., Staude, J.M. (1991): Fluid channelling during ductile shearing:
607 transformation of granodiorite into aluminous schist in the Tauren Window, Eastern Alps. *J.*
608 *Metamorph. Geol.*, **9**, 419–431.

609 Smye, A.J., Greenwood, L.V., Holland, T.J.B. (2010): Garnet–chloritoid–kyanite assemblages: eclogite
610 facies indicators of subduction constraints in orogenic belts. *J. Metamorph. Geol.*, **28**, 753–768.

611 Theye, T. & Seidel, E. (1991): Petrology of low-grade high pressure metapelites from the External
612 Hellenides (Crete, Peloponnese). A case study with attention to sodic minerals. *Eur. J. Mineral.*, **3**,
613 343–366.

614 Vidal, O. & Theye, T. (1996): Petrology of Fe-Mg-carpholite-bearing metasediments from NE Oman. *J.*
615 *Metamorph. Geol.*, **14**, 381–397.

616 Warren, C.J. & Waters, D.J. (2006): Oxidized eclogites and garnet-blueschists from Oman: P–T path
617 modelling in the NCFMASHO system. *J. Metamorph. Geol.*, **24**, 783–802.

618 Wei, C., Wang, W., Clarke, G.L., Zhang, L., Song, S. (2009): Metamorphism of high/ultrahigh-pressure
619 pelitic-felsic schist in the South Tianshan Orogen, NW China: phase equilibria and P-T path. *J.*
620 *Petrol.*, **50**, 1973–1991.

621 Wei, C.J. & Powell, R. (2004): Calculated phase relations in high-pressure metapelites in the system
622 NCFMASH (Na₂O–K₂O–FeO–MgO–Al₂O₃–SiO₂–H₂O) with application to natural rocks. *J. Petrol.*, **44**,
623 183–202.

624 Wei, C.J. & Powell, R. (2006): Calculated phase relations in the system NCKFMASH (Na₂O–CaO–K₂O–
625 FeO–MgO–Al₂O₃–SiO₂–H₂O) for high-pressure metapelites. *J. Petrol.*, **47**, 385–408.

626 Wei, C.J. & Song, S.G. (2008): Chloritoid-glaucophane schist in the north Qilian orogen, NW China:
627 phase equilibria and P-T path from garnet zonation. *J. Metamorph. Geol.*, **26**, 301–316.

628 White, R., Pomroy, N., Powell, R. (2005): An in-situ metatexite– diatexite transition in upper
629 amphibolite facies rocks from Broken Hill, Australia. *J. Metamorph. Geol.*, **23**, 579–602.

630 Whitney, D.L. & Evans, B.W. (2010): Abbreviations for names of rock-forming minerals. *Am. Mineral.*,
631 **95**, 185–187.

632

633 **Figure captions**

634

635 **Fig. 1 – (a)** Tectonic sketch map of the southern Dora-Maira Massif, with the location of Costigliole
636 Saluzzo (modified from Castelli *et al.*, 2014). **(b)** The roman villa at Costigliole Saluzzo (from Elia *et al.*,
637 2013; in red: room H2, where the majority of the querns come from). **(c)** A quern stone during its
638 excavation.

639

640 **Fig. 2 – (a, b)** Rotary querns from Costigliole Saluzzo (a: specimen from US900; b: specimen from
641 US773). **(c)** Reconstruction of a quern (from Donner & Marzoli, 1994) **(d, e, f)** Details of specimens
642 from US773 (d), US900 (e) and US557 (f).

643

644 **Fig. 3 –** Processed major elements μ -XRF maps of the whole thin sections of samples US900 and
645 US773.

646

647 **Fig. 4 – (a, b)** Representative microstructures of samples US900 (a) and US773 (b) (Plane Polarized
648 Light: PPL). **(c, d)** Garnet porphyroblasts with coesite (partially inverted to quartz) inclusion in the rim
649 and chloritoid inclusion in the core (c: US900; d: US773) (PPL). **(e)** Zoned glaucophane nematoblasts
650 associated to blue-green chloritoid (US900) (PPL). **(f)** Slightly zoned blue-green chloritoid partially
651 replaced by greenish Mg-chlorite (US773) (PPL). Mineral abbreviations after Whitney & Evans (2010).

652

653 **Fig. 5 – (a-c)** Glaucophane composition plotted in the Si vs. $Mg/(Mg+Fe^{+2})$ (a), Si vs. Fe^{+3}/Fe_{tot} , and Si
654 vs. $Na/(Na+Ca)$ diagrams (data from both samples US900 and US773). **(d)** Chloritoid composition
655 plotted in the $(Fe^{+2}+Mg)-(Al^{VI}+Fe^{+3})-Mg$ diagram (data from both samples US900 and US773).

656

657 **Fig. 6 – (a)** Garnet composition plotted in the Prp-Alm-(Sps+Grs) diagram (data from both samples
658 US900 and US773). **(b)** Major and trace element chemical profile of a garnet porphyroblast from
659 sample US900. Note the bell shaped profile of X_{Mn} , suggesting a prograde growth and the similar
660 pattern of Y, Na and Cr.

661

662 **Fig. 7 – (a)** Microphotograph of large and relatively well preserved coesite inclusion within garnet
663 mantle, and smaller polycrystalline quartz inclusions within garnet rim (US773; crossed polarized
664 light). **(b)** Microphotograph of relatively small coesite inclusion, partly inverted to palisade quartz,
665 within garnet rim (US773) (PPL). **(c)** Raman spectrum of coesite (US773). **(d)** Microphotograph of the
666 mapped, well preserved coesite inclusion in garnet. The rectangle shows the mapped area reported
667 in Fig. 7e (US773) (PPL). **(d)** Raman map of the spatial distribution and the intensity of the main peaks
668 of coesite (524 cm^{-1} , in green), quartz (470 cm^{-1} , in blue), and garnet (917 cm^{-1} , in red). From the map
669 is evident that the coesite inversion to quartz start from the grain-boundaries and the fractures.

670

671 **Fig. 8 – (a)** P-T pseudosection calculated for sample US900 in the MnNCFMASH system using the
672 whole rock bulk composition (Table 3). The variance of the fields varies from three (i.e. 7 phases,
673 light grey fields) to six (i.e. 4 phases, darker grey fields). Pink continuous, dashed and dotted lines are
674 the X_{Mg} , X_{Ca} and X_{Mn} isopleths of garnet corresponding to the measured composition of garnet core;
675 light blue continuous line is the X_{Mg} isopleth of chloritoid corresponding to the measured
676 composition of chloritoid core. P-T conditions constrained for the growth of garnet core are
677 represented by the white dotted polygon. **(b)** P-T pseudosection calculated for sample US900 using

678 the fractionated bulk composition (whole rock composition minus garnet core and mantle; Table 3).
679 The variance of the fields varies from three (i.e. 7 phases, light grey fields) to six (i.e. 4 phases, darker
680 grey fields). Pink continuous, and dashed lines are the X_{Mg} and X_{Ca} isopleths of garnet corresponding
681 to the measured composition of garnet rim; light blue continuous line is the X_{Mg} isopleth of chloritoid
682 corresponding to the measured composition of chloritoid rim. P-T conditions constrained for the
683 growth of garnet rim are represented by the white dotted polygon. **(c-l)** Modal variations (vol%) of
684 the main mineral phases in sample US900 (c-i) and isomodes of water (mol) (l) calculated for the P-T
685 pseudosection of Fig. 8b. Colours from blue to red imply higher modal proportions as indicated in
686 each legend. The black arrow is the prograde P-T path constrained basing on the pseudosection
687 results and YAG thermometry.

688

689 **Fig. 9** – Prograde P-T path (black arrow) inferred for the studied samples basing on the
690 pseudosection results and YAG thermometry and comparison with the P-T evolution constrained for
691 the adjacent UHP Brossasco-Isasca Unit (dashed grey arrow). The blue and light blue polygons
692 represent the P-T conditions constrained for the growth of garnet core and rim, respectively (see Fig.
693 8a, b).

694

695

696

Figure 1

[Click here to download Figure: Fig1.tif](#)

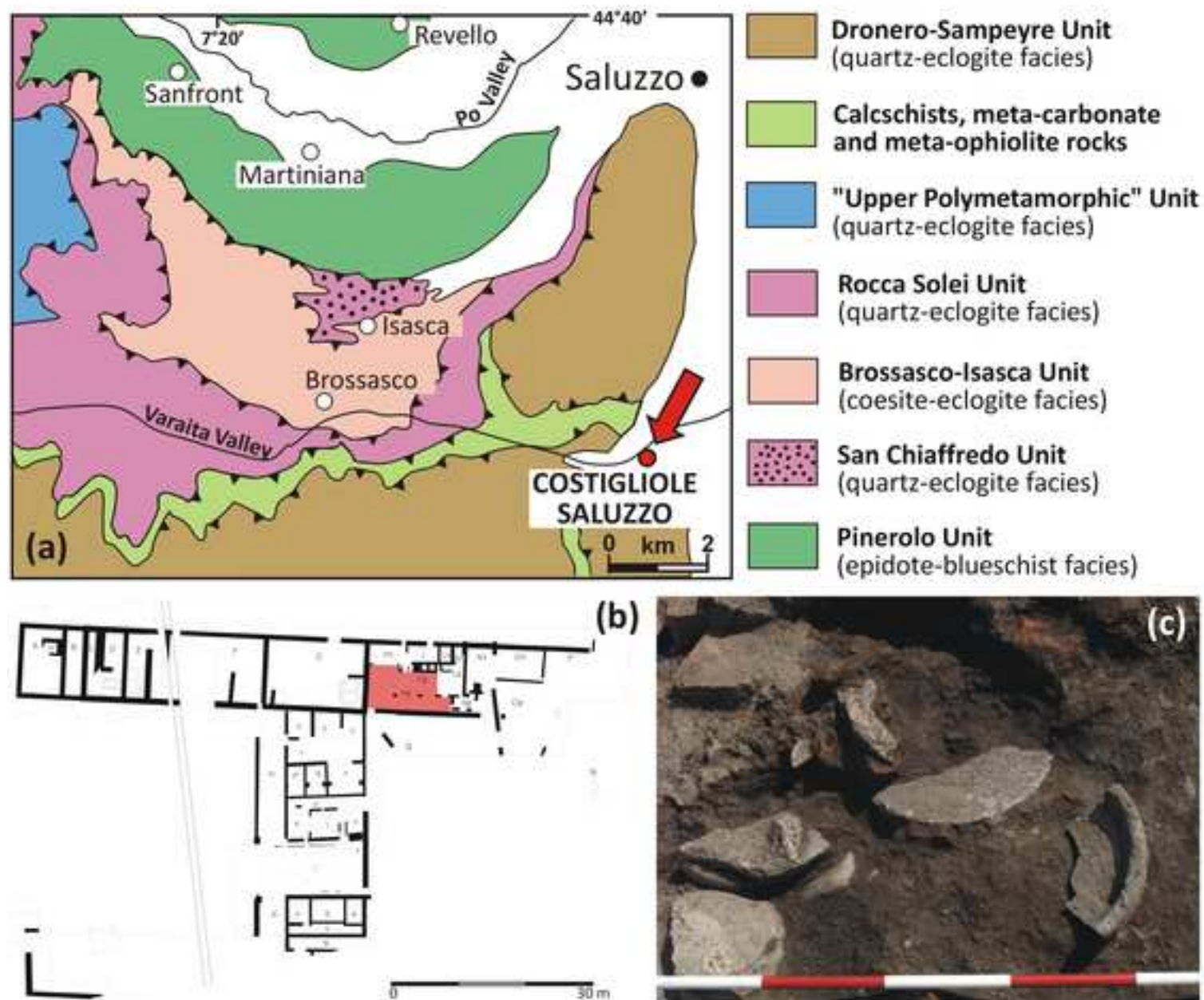


Fig. 1. (a) Tectonic sketch map of the southern Dora-Maira Massif, with the location of Costigliole Saluzzo (modified from Castelli et al., 2014). (b) The roman villa at Costigliole Saluzzo (from Eila et al., 2013; in red; room HQ, where the majority of the querns come from). (c) A quern stone during its excavation.

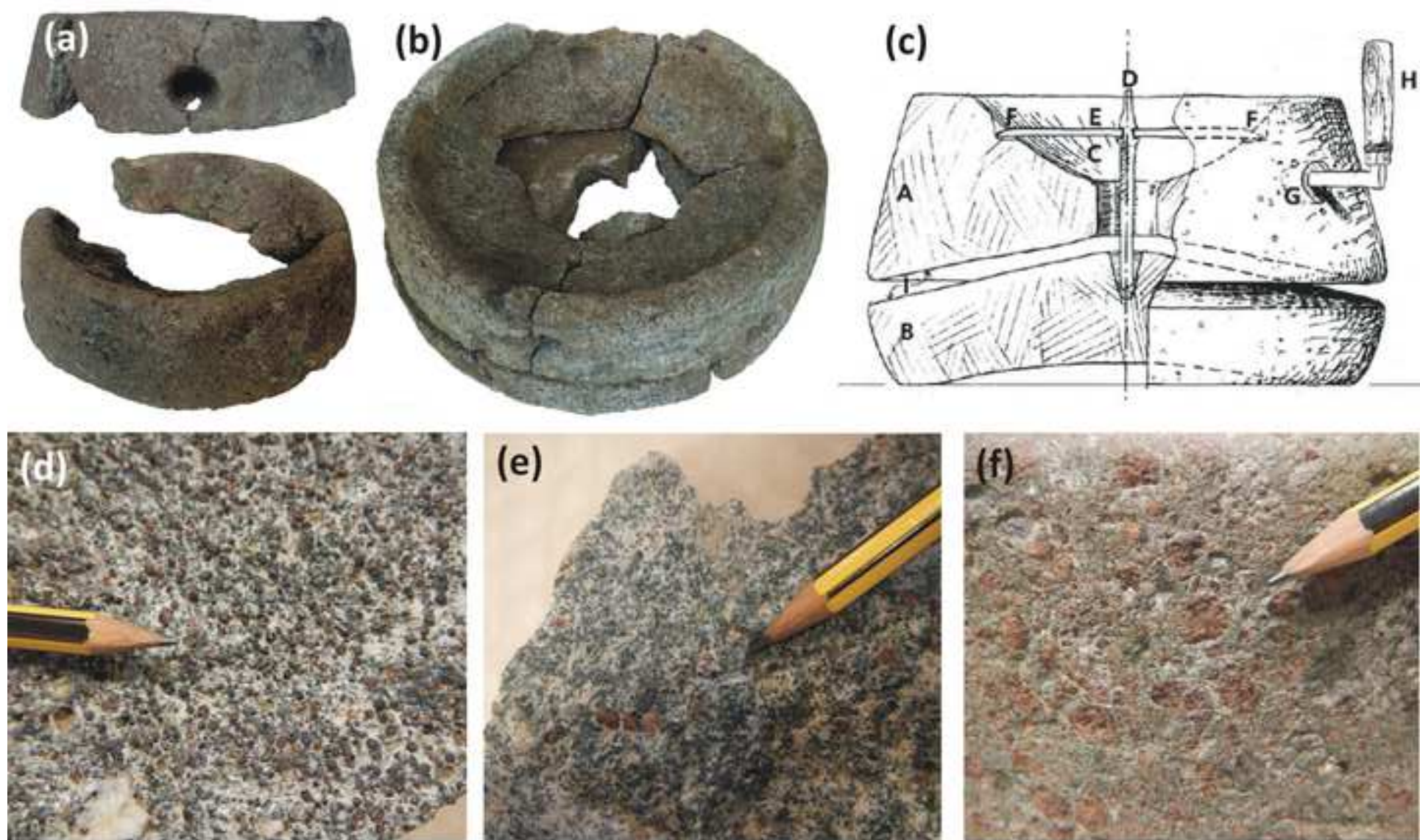


Fig. 2 (a, b) Rotary querns from Costigliole Saluzzo (a: specimen from US900; b: specimen from US773). (c) Reconstruction of a quern (from Donner & Marzoli, 1994) (d, e, f) Details of specimens from US773 (d), US900 (e) and US557 (f).

Figure 3

[Click here to download Figure: Fig3.tif](#)

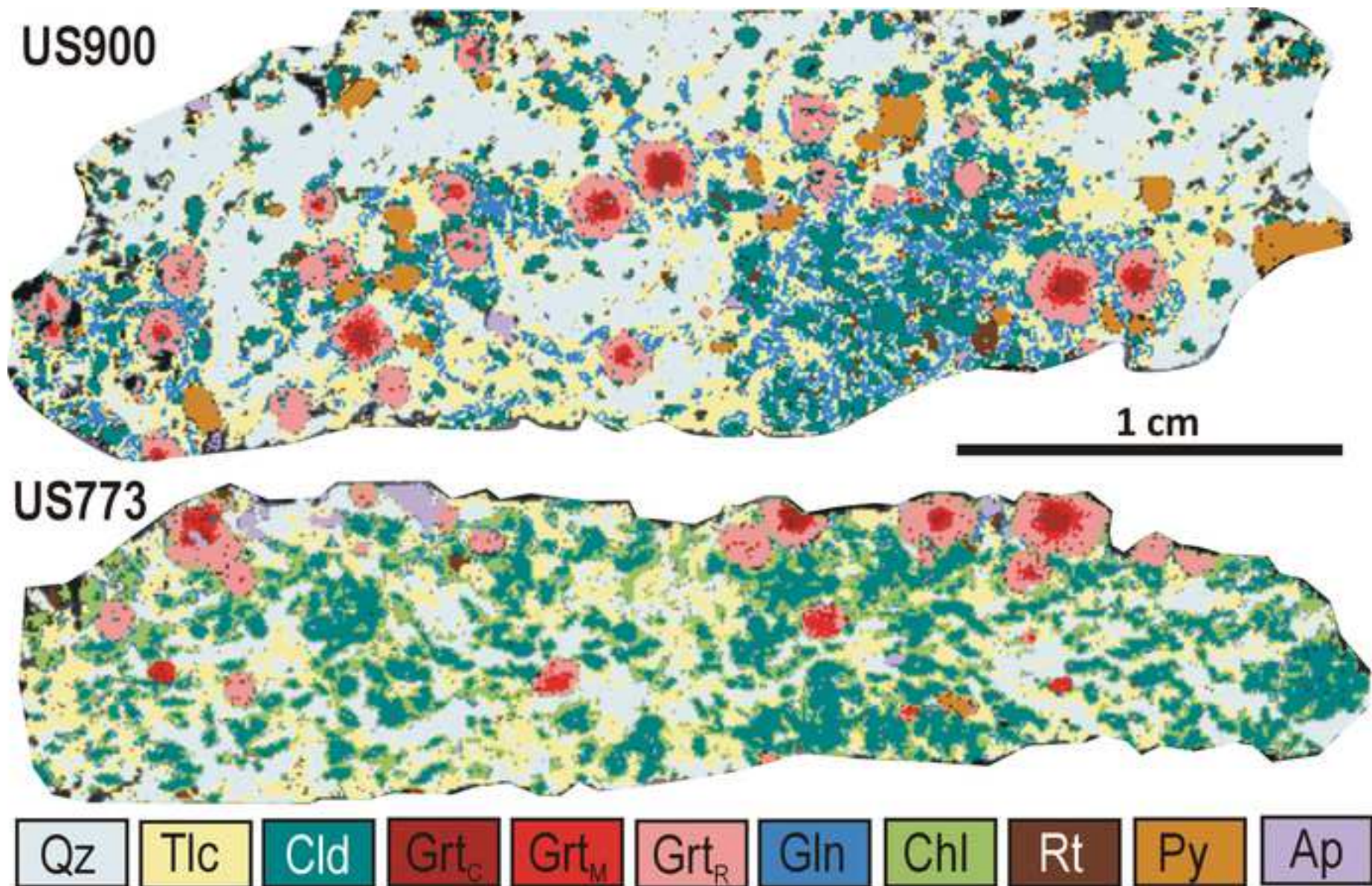


Fig. 3 Processed major elements μ -XRF maps of the whole thin sections of samples US900 and Us773.

Figure 4
Click here to download Figure: Fig4.tif

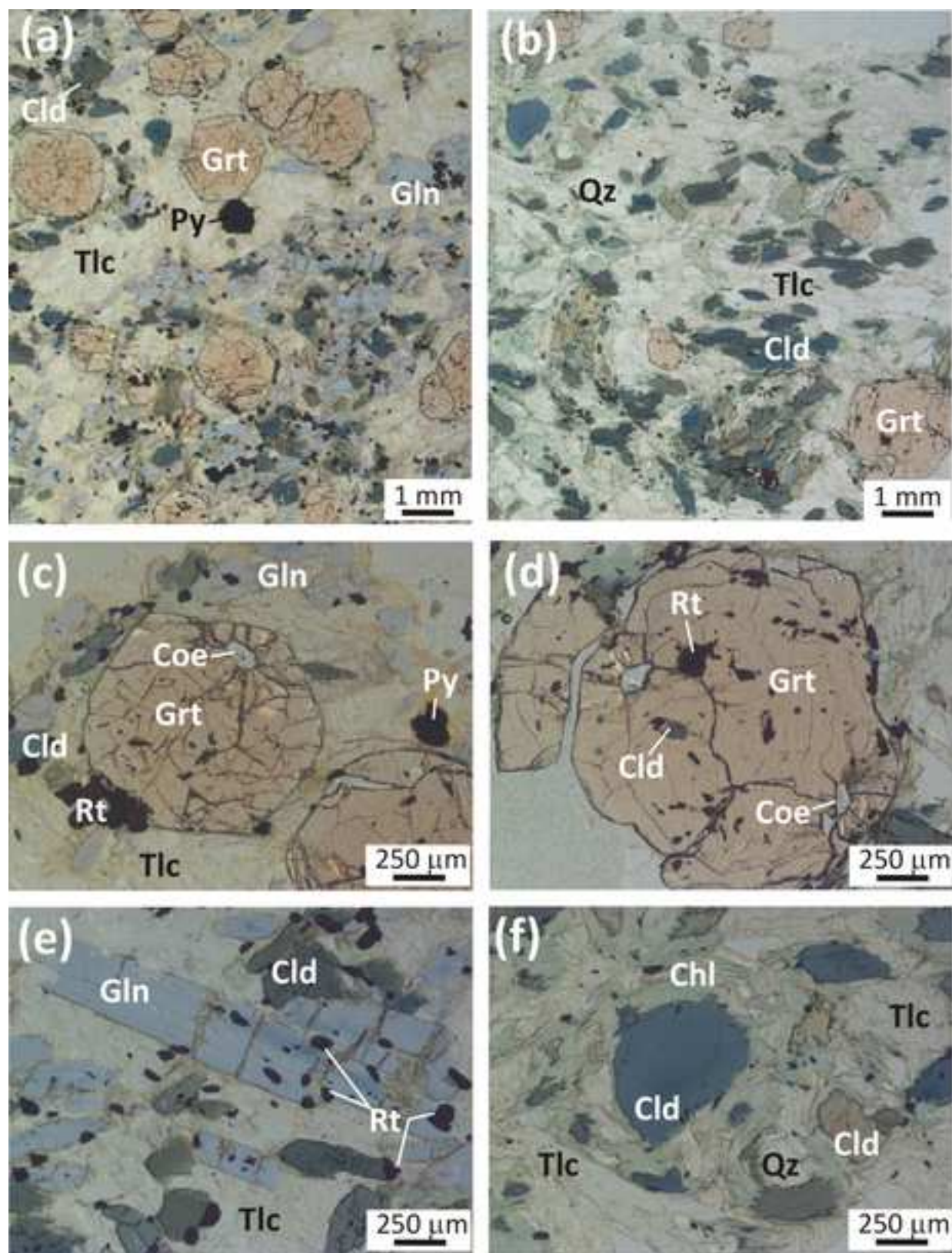


Fig. 4 (a, b) Representative microstructures of samples US900 (a) and US773 (b) (Plane Polarized Light: PPL). (c, d) Garnet porphyroblasts with coesite [partially inverted to quartz] inclusion in the rim and chloritoid inclusion in the core (c: US900; d: US773) (PPL). (e) Zoned glaucophane nematoblasts associated to blue-green chloritoid (US900) (PPL). (f) Slightly zoned blue-green chloritoid partially replaced by greenish Mg-chlorite (US773) (PPL). Mineral abbreviations after Whitney & Evans (2010).

Figure 5
[Click here to download Figure: Fig5.tif](#)

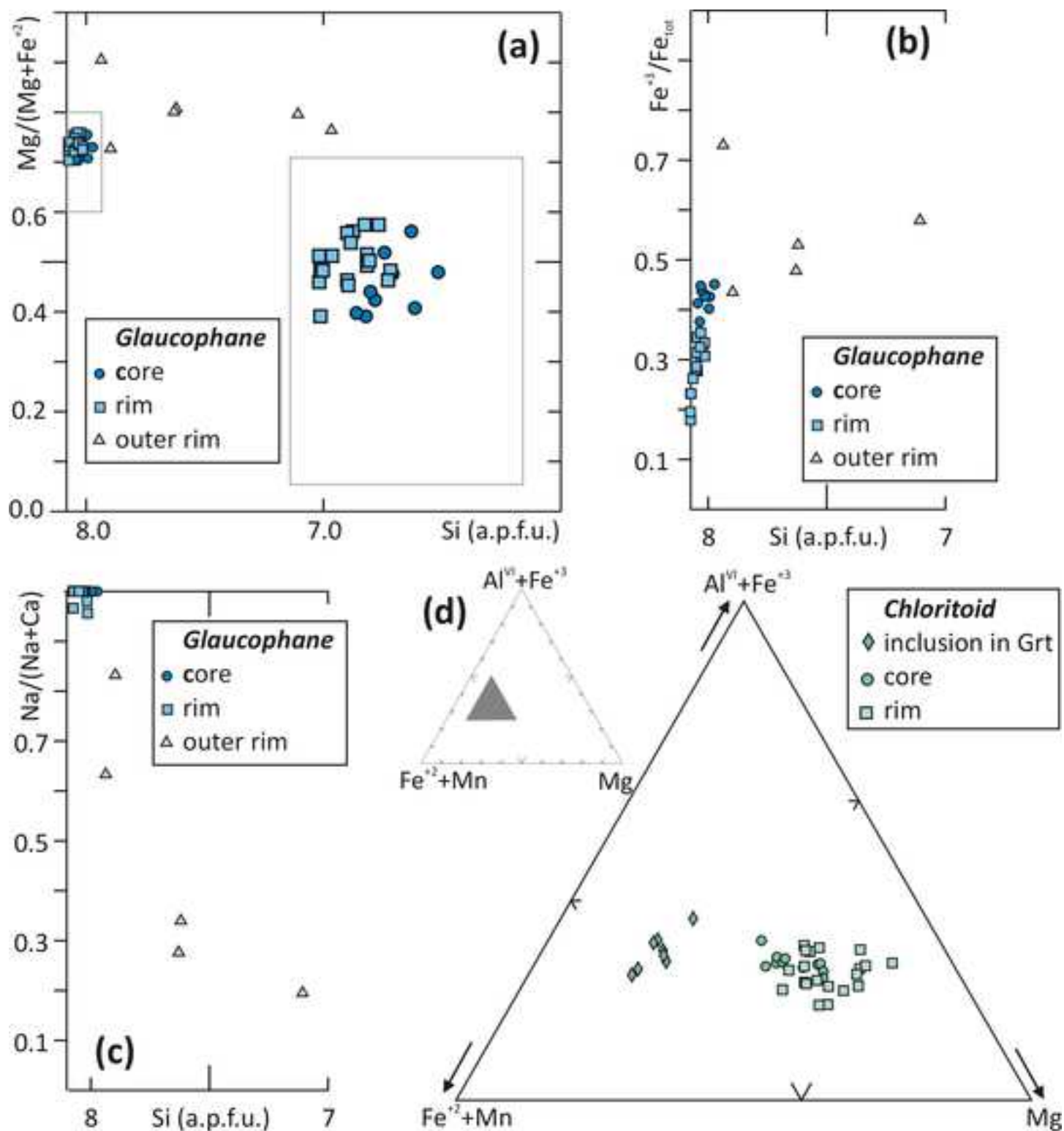


Fig. 5 (a-c) Glaucophane composition plotted in the Si vs. Mg/(Mg+Fe³⁺) (a), Si vs. Fe³⁺/Fe_{tot}, and Si vs. Na/(Na+Ca) diagrams (data from both samples US900 and US773). **(d)** Chloritoid composition plotted in the (Fe²⁺+Mg)-(Al^{VI}+Fe³⁺)-Mg diagram (data from both samples US900 and US773).

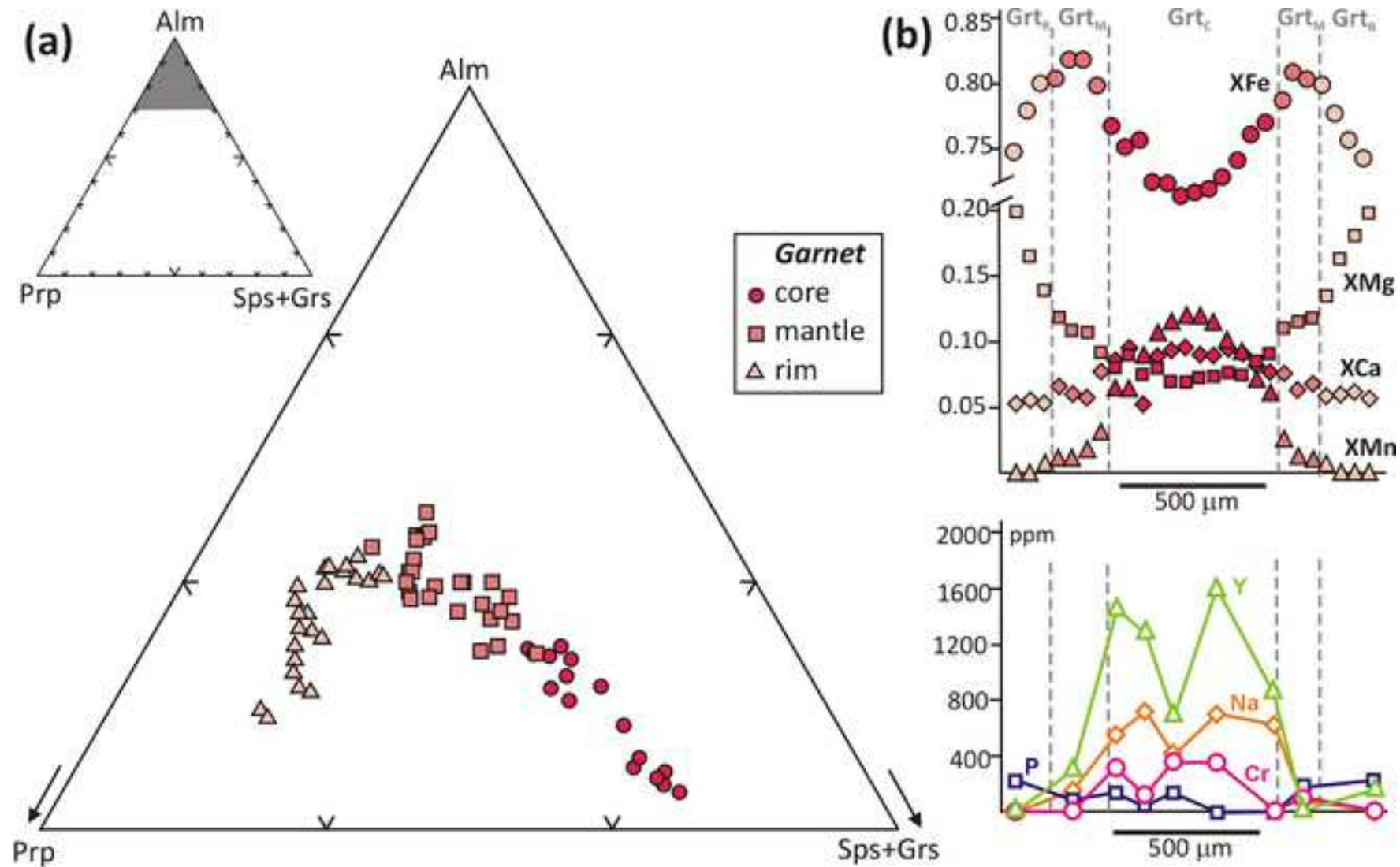


Fig. 6 (a) Garnet composition plotted in the Prp-Alm-(Sps+Grs) diagram (data from both samples US900 and US773). (b) Major and trace element chemical profile of a garnet porphyroblast from sample US900. Note the bell shaped profile of X_{Fe} , suggesting a prograde growth and the similar pattern of Y, Na and Cr.

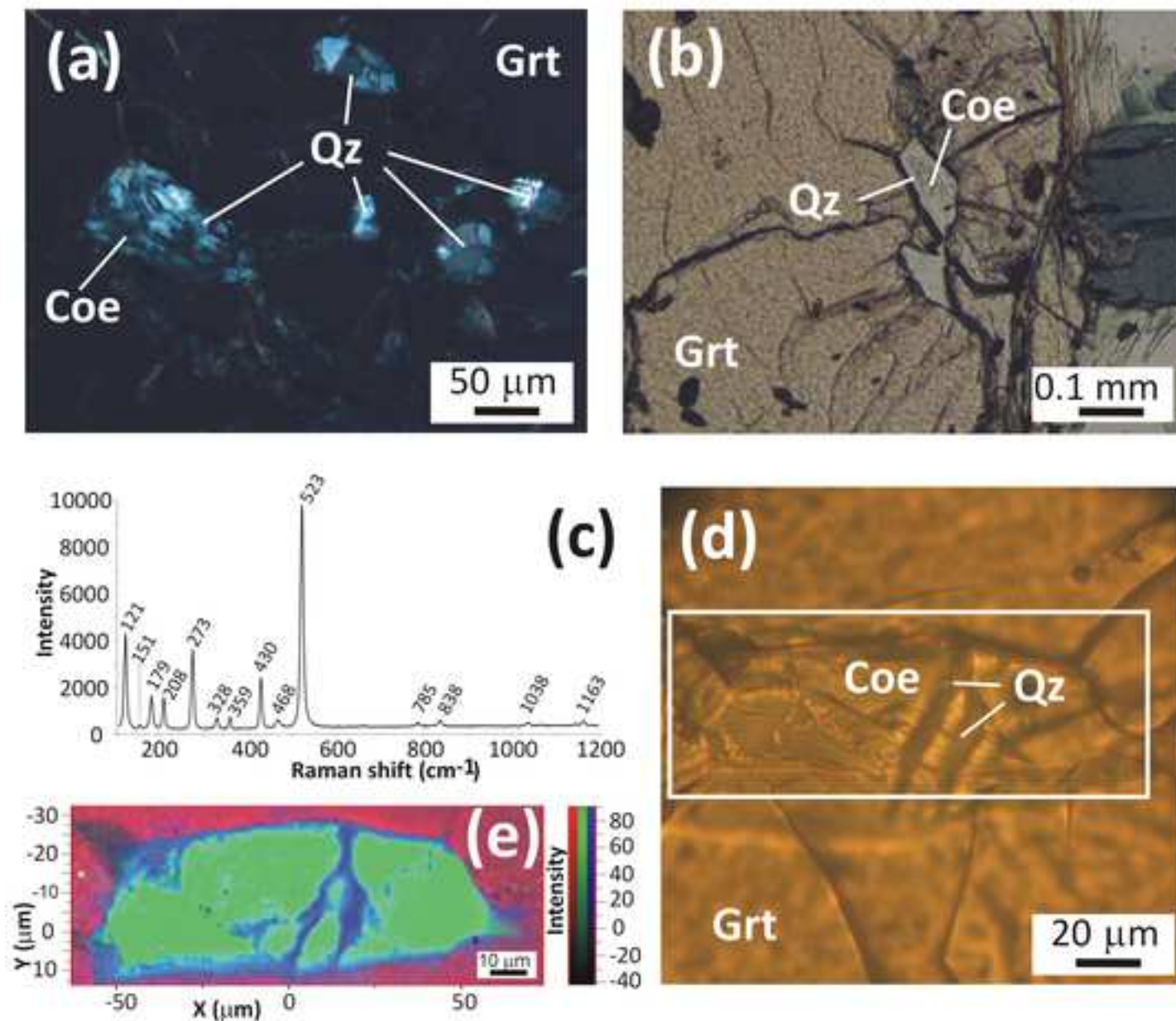


Fig. 7 (a) Microphotograph of large and relatively well preserved coesite inclusion within garnet mantle, and smaller polycrystalline quartz inclusions within garnet rim (US773; crossed polarized light). (b) Microphotograph of relatively small coesite inclusion, partly inverted to palisade quartz, within garnet rim (US773) (PPL). (c) Raman spectrum of coesite (US773). (d) Microphotograph of the mapped, well preserved coesite inclusion in garnet. The rectangle shows the mapped area reported in Fig. 7e (US773) (PPL). (e) Raman map of the spatial distribution and the intensity of the main peaks of coesite (524 cm⁻¹, in green), quartz (470 cm⁻¹, in blue), and garnet (917 cm⁻¹, in red). From the map is evident that the coesite inversion to quartz start from the grain-boundaries and the fractures.

Figure 8

[Click here to download Figure: Fig8.tif](#)

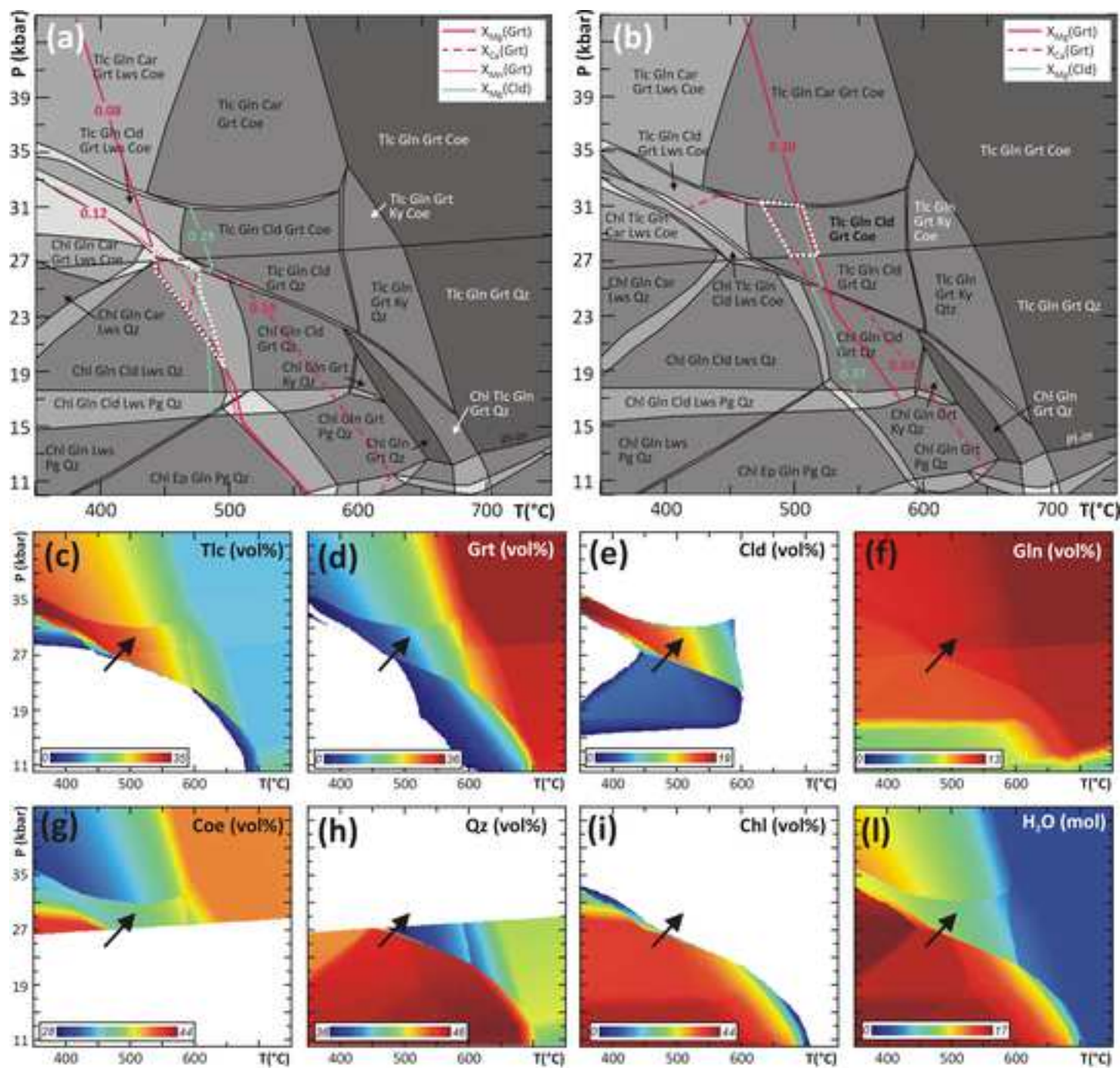


Fig. 8 (a) P-T pseudosection calculated for sample US900 in the MnNCFMASH system using the whole rock bulk composition (Table 3). The variance of the fields varies from three (i.e. 7 phases, light grey fields) to six (i.e. 4 phases, darker grey fields). Pink continuous, dashed and dotted lines are the X_{Mg} , X_{Ca} and X_{Mn} isopleths of garnet corresponding to the measured composition of garnet core; light blue continuous line is the X_{Mg} isopleth of chloritoid corresponding to the measured composition of chloritoid core. P-T conditions constrained for the growth of garnet core are represented by the white dotted polygon. (b) P-T pseudosection calculated for sample US900 using the fractionated bulk composition (whole rock composition minus garnet core and mantle; Table 3). The variance of the fields varies from three (i.e. 7 phases, light grey fields) to six (i.e. 4 phases, darker grey fields). Pink continuous, and dashed lines are the X_{Mg} and X_{Ca} isopleths of garnet corresponding to the measured composition of garnet rim; light blue continuous line is the X_{Mg} isopleth of chloritoid corresponding to the measured composition of chloritoid rim. P-T conditions constrained for the growth of garnet rim are represented by the white dotted polygon. (c-l) Modal variations (vol%) of the main mineral phases in sample US900 (c-i) and isomodes of water (mol) (l) calculated for the P-T pseudosection of Fig. 8b. Colours from blue to red imply higher modal proportions as indicated in each legend. The black arrow is the prograde P-T path constrained basing on the pseudosection results and YAG thermometry.

Figure 9

[Click here to download Figure: Fig9.tif](#)

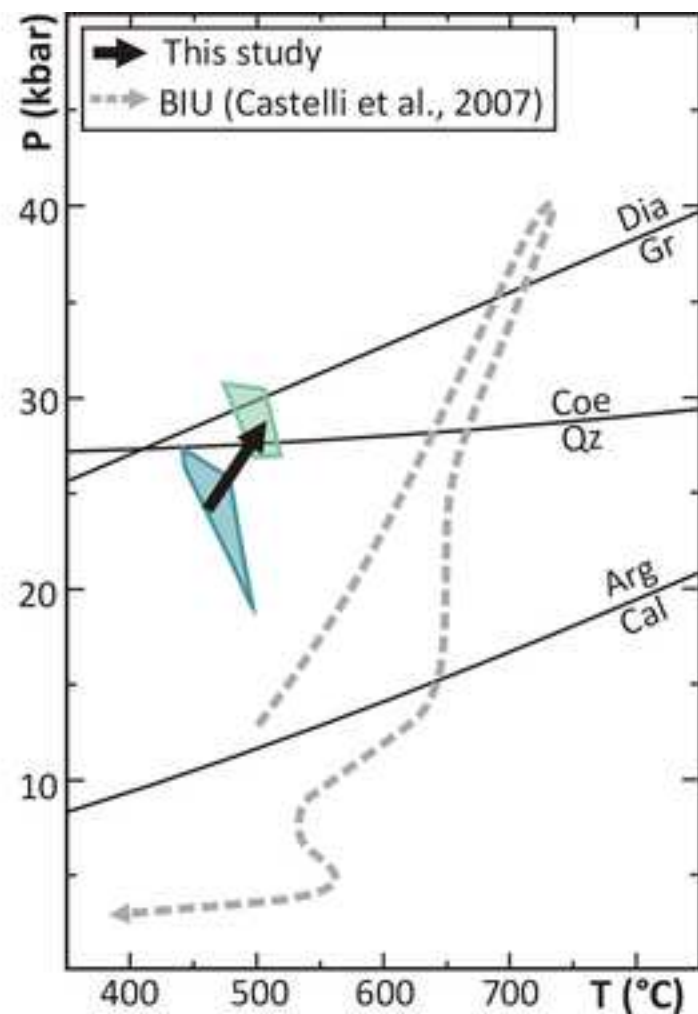


Fig. 9 Prograde P-T path (black arrow) inferred for the studied samples basing on the pseudosection results and YAG thermometry and comparison with the P-T evolution constrained for the adjacent UHP Brossasco-Isasca Unit (dashed grey arrow). The blue and light blue polygons represent the P-T conditions constrained for the growth of garnet core and rim, respectively (see Fig. 8a, b).

Table 1. Representative WDS a

Sample Analysis	US900									773_1 rim
	900_23 rim	900_24 mantle	900_25	900_26	900_27 core			900_28	900_29	
SiO ₂	37.52	36.86	37.40	37.01	36.60	36.88	37.14	36.89	37.32	37.67
P ₂ O ₅	0.05	0.02	0.03	0.01	0.03	0.00	0.00	0.04	0.05	0.01
TiO ₂	0.00	0.04	0.00	0.08	0.10	0.07	0.02	0.08	0.02	0.05
Al ₂ O ₃	21.16	20.61	20.88	20.62	20.56	20.67	20.70	20.77	21.50	21.12
Cr ₂ O ₃	0.00	0.00	0.05	0.02	0.05	0.05	0.00	0.01	0.00	0.00
Y ₂ O ₃	0.00	0.04	0.18	0.16	0.08	0.20	0.11	0.00	0.02	0.00
FeO	34.93	37.01	35.15	33.06	32.19	33.34	34.55	36.73	34.33	35.23
MnO	0.16	0.54	1.80	4.01	4.77	4.34	2.80	0.47	0.16	0.18
MgO	4.40	2.77	2.34	1.96	1.79	1.93	2.18	2.89	4.72	4.48
NiO	0.00	0.03	0.02	0.00	0.24	0.00	0.00	0.00	0.11	0.00
CaO	1.90	2.01	2.70	2.79	3.10	2.80	2.60	2.17	2.00	1.70
Na ₂ O	0.00	0.02	0.07	0.10	0.06	0.09	0.09	0.01	0.00	0.00
K ₂ O	0.00	0.00	0.00	0.02	0.00	0.00	0.01	0.01	0.01	0.01
Total	100.10	99.95	100.62	99.83	99.56	100.36	100.19	100.06	100.22	100.44
Si	2.988	2.979	3.003	3.001	2.979	2.979	2.999	2.974	2.960	2.992
P	0.003	0.001	0.002	0.001	0.002	0.000	0.000	0.003	0.003	0.001
Ti	0.000	0.002	0.000	0.005	0.006	0.004	0.001	0.005	0.001	0.003
Al	1.986	1.964	1.976	1.971	1.972	1.967	1.969	1.973	2.010	1.977
Cr	0.000	0.000	0.003	0.001	0.003	0.003	0.000	0.001	0.000	0.000
Y	0.000	0.002	0.008	0.007	0.004	0.009	0.005	0.000	0.001	0.000
Fe ⁺³	0.033	0.073	0.015	0.025	0.056	0.069	0.041	0.069	0.063	0.034
Fe ⁺²	2.293	2.429	2.345	2.217	2.135	2.183	2.292	2.407	2.214	2.306
Mn	0.010	0.037	0.123	0.275	0.329	0.297	0.192	0.032	0.011	0.012
Mg	0.522	0.334	0.281	0.237	0.217	0.233	0.262	0.348	0.558	0.531
Ni	0.000	0.002	0.001	0.000	0.016	0.000	0.000	0.000	0.007	0.000
Ca	0.162	0.174	0.232	0.242	0.270	0.243	0.225	0.187	0.170	0.144
Na	0.000	0.003	0.011	0.015	0.009	0.014	0.014	0.002	0.000	0.000
K	0.000	0.000	0.000	0.002	0.000	0.000	0.001	0.001	0.001	0.001
XMg	0.18	0.11	0.09	0.08	0.08	0.08	0.09	0.12	0.19	0.18
XFe	0.77	0.82	0.78	0.74	0.72	0.74	0.77	0.81	0.75	0.77
XCa	0.05	0.06	0.08	0.08	0.09	0.08	0.08	0.06	0.06	0.05
XMn	0.00	0.01	0.04	0.09	0.11	0.10	0.06	0.01	0.00	0.00

Structural formulae have been calculated on the basis of 12 oxygens. Fe⁺³ has been calculated by stoichiometry.

analysis of garnet

US773										
m	773_2	773_3	773_4 mantle	773_5	773_6 core	773_7	773_8 mantle	773_9	773_10 rim	773_11
	36.99	36.84	36.93	37.21	36.82	36.85	36.91	37.19	37.18	37.68
	0.05	0.09	0.01	0.05	0.00	0.04	0.00	0.00	0.12	0.00
	0.07	0.07	0.11	0.05	0.07	0.05	0.17	0.06	0.01	0.15
	20.67	20.63	20.19	20.40	20.34	20.72	20.49	20.73	20.96	21.28
	0.00	0.05	0.04	0.04	0.05	0.01	0.07	0.00	0.00	0.00
	0.00	0.12	0.02	0.00	0.25	0.00	0.02	0.00	0.00	0.00
	36.50	36.96	36.80	35.86	34.39	35.78	35.86	36.47	35.91	34.84
	0.16	0.32	0.58	1.23	2.72	1.15	0.37	0.19	0.11	0.12
	3.72	2.82	2.41	2.29	2.22	2.52	2.94	3.33	4.00	4.62
	0.00	0.00	0.14	0.00	0.05	0.09	0.17	0.13	0.14	0.00
	1.50	2.54	2.87	3.01	3.12	2.89	2.62	2.08	1.48	1.84
	0.00	0.03	0.02	0.00	0.07	0.03	0.00	0.04	0.03	0.01
	0.00	0.00	0.00	0.01	0.00	0.02	0.00	0.02	0.02	0.01
	99.64	100.47	100.12	100.15	100.09	100.15	99.63	100.23	99.95	100.55
	2.981	2.959	2.986	3.004	2.979	2.970	2.986	2.983	2.977	2.984
	0.003	0.006	0.000	0.003	0.000	0.003	0.000	0.000	0.008	0.000
	0.004	0.004	0.007	0.003	0.004	0.003	0.011	0.004	0.001	0.009
	1.963	1.953	1.924	1.942	1.939	1.967	1.954	1.960	1.978	1.986
	0.000	0.003	0.003	0.003	0.003	0.001	0.004	0.000	0.000	0.000
	0.000	0.005	0.001	0.000	0.011	0.000	0.001	0.000	0.000	0.000
	0.062	0.108	0.090	0.037	0.091	0.089	0.048	0.075	0.061	0.030
	2.398	2.375	2.398	2.384	2.235	2.323	2.378	2.372	2.343	2.278
	0.011	0.022	0.040	0.084	0.186	0.078	0.025	0.013	0.007	0.008
	0.447	0.338	0.291	0.276	0.267	0.303	0.355	0.399	0.477	0.546
	0.000	0.000	0.009	0.000	0.003	0.006	0.011	0.008	0.009	0.000
	0.130	0.219	0.249	0.260	0.270	0.250	0.227	0.179	0.127	0.156
	0.000	0.005	0.003	0.000	0.011	0.005	0.000	0.006	0.005	0.002
	0.000	0.000	0.000	0.001	0.000	0.002	0.000	0.002	0.002	0.001
	0.15	0.11	0.10	0.09	0.09	0.10	0.12	0.14	0.16	0.18
	0.80	0.80	0.80	0.79	0.75	0.78	0.79	0.80	0.79	0.76
	0.04	0.07	0.08	0.09	0.09	0.08	0.08	0.06	0.04	0.05
	0.00	0.01	0.01	0.03	0.06	0.03	0.01	0.00	0.00	0.00

Table 2. Representative SEM-EDS analysis of chloritoid, g

Chloritoid						Amphibole			
Sample Analysis	US900		US773			Sample Analysis	US900		
	2Ctd2 core	2Ctd3 rim	1Ctd46 in Grt	2Ctd11 core	2Ctd12 rim		2Gln8 core	2Gln9 rim	1Gln60 core
SiO ₂	24.79	24.87	24.20	24.51	24.75	SiO ₂	56.30	56.22	56.25
Al ₂ O ₃	38.80	38.57	37.78	37.57	37.70	Al ₂ O ₃	8.24	9.46	7.60
FeO	22.97	22.17	26.81	24.70	23.35	FeO	12.38	8.91	13.09
MnO	0.00	0.00	0.00	0.00	0.00	MnO	0.00	0.00	0.00
MgO	5.47	6.25	3.54	4.84	5.89	MgO	10.27	11.04	10.32
CaO	0.00	0.00	0.00	0.00	0.00	CaO	0.00	0.00	0.00
Na ₂ O	0.00	0.00	0.00	0.00	0.00	Na ₂ O	6.58	6.70	6.53
K ₂ O	0.00	0.00	0.00	0.00	0.00	K ₂ O	0.00	0.00	0.00
Total	92.03	91.86	92.33	91.61	91.68	Total	95.87	94.42	95.89
Si	2.027	2.026	2.008	2.029	2.031	Si	8.035	8.051	8.043
Al	3.737	3.704	3.694	3.664	3.646	Al	1.386	1.597	1.281
Fe ⁺³	0.210	0.244	0.290	0.278	0.292	Fe ⁺³	0.555	0.299	0.646
Fe ⁺²	1.360	1.267	1.570	1.432	1.311	Fe ⁺²	0.922	0.768	0.920
Mn	0.000	0.000	0.000	0.000	0.000	Mn	0.000	0.000	0.00
Mg	0.666	0.759	0.438	0.597	0.720	Mg	2.185	2.357	2.200
Ca	0.000	0.000	0.000	0.000	0.000	Ca	0.000	0.000	0.000
Na	0.000	0.000	0.000	0.000	0.000	Na	1.821	1.860	1.810
K	0.000	0.000	0.000	0.000	0.000	K	0.000	0.000	0.000
XMg	0.33	0.38	0.22	0.29	0.36	XMg	0.70	0.75	0.71
XFe ⁺³	0.05	0.06	0.07	0.07	0.07	XFe ⁺³	0.29	0.16	0.34

Structural formulae have been calculated on the basis of 14 oxygens for chloritoid, 13CNK (Si+Al+Mg+Ti+Mn+Fe=13) for amphibole. Fe⁺³ has been calculated by stoichiometry except for amphibole (average Fe⁺³ values).

laucophane, talc and Mg-chlorite

US773		Sample Analysis	Talc		Chlorite	
1Gln62 rim	1Gln70 o-rim		US900 1Tlc27	US773 2Tlc23	US773 2Chl21	
56.97	54.71	SiO ₂	61.53	61.49	SiO ₂	27.95
9.43	4.32	Al ₂ O ₃	0.00	0.00	Al ₂ O ₃	20.06
9.39	10.76	FeO	6.94	6.99	FeO	17.31
0.00	0.00	MnO	0.00	0.00	MnO	0.00
11.08	15.56	MgO	26.50	26.19	MgO	22.05
0.00	3.01	CaO	0.00	0.00	CaO	0.00
6.68	2.87	Na ₂ O	0.00	0.00	Na ₂ O	0.00
0.00	0.00	K ₂ O	0.00	0.00	K ₂ O	0.00
95.67	93.30	Total	94.97	94.67	Total	87.36
8.064	7.937	Si	4.032	4.046	Si	2.825
1.573	0.739	Al	0.000	0.000	Al	2.390
0.291	0.953	Fe ⁺³	0.000	0.000	Fe ⁺³	0.000
0.821	0.352	Fe ⁺²	0.380	0.385	Fe ⁺²	1.463
0.00	0.00	Mn	0.000	0.000	Mn	0.000
2.338	3.365	Mg	2.588	2.569	Mg	3.322
0.000	0.468	Ca	0.000	0.000	Ca	0.000
1.833	0.807	Na	0.000	0.000	Na	0.000
0.000	0.000	K	0.000	0.000	K	0.000
0.74	0.91	XMg	0.87	0.87	XMg	0.69
0.16	0.56					

or amphibole, 12 oxygens for talc and 18 oxygens for chlorite.

Table 3. Bulk compositions (wt%) and modal amounts (vol%) of the main mineral phases

Sample	US900	US900*	US773
SiO ₂	66.45	67.01	51.56
Al ₂ O ₃	10.49	10.3	18.52
MgO	10.67	10.84	13.37
CaO	0.21	0.17	0.19
MnO	0.08	0.01	0.06
FeO	10.13	9.65	14.92
Fe ₂ O ₃	1.05	1.08	1.09
Na ₂ O	0.93	0.95	0.29
Total	100.0	100.0	100.0
Qz/Coe	38.4		21.4
Tlc	30.5		22.3
Cld	14.0		22.6
Grt	7.9		8.1
Gln	9.2		2.8
Mg-Chl	<1		22.8

* effective bulk composition in equilibrium during the growth of Grt rim (whole rock composition minus the garnet core and mantle compositions)

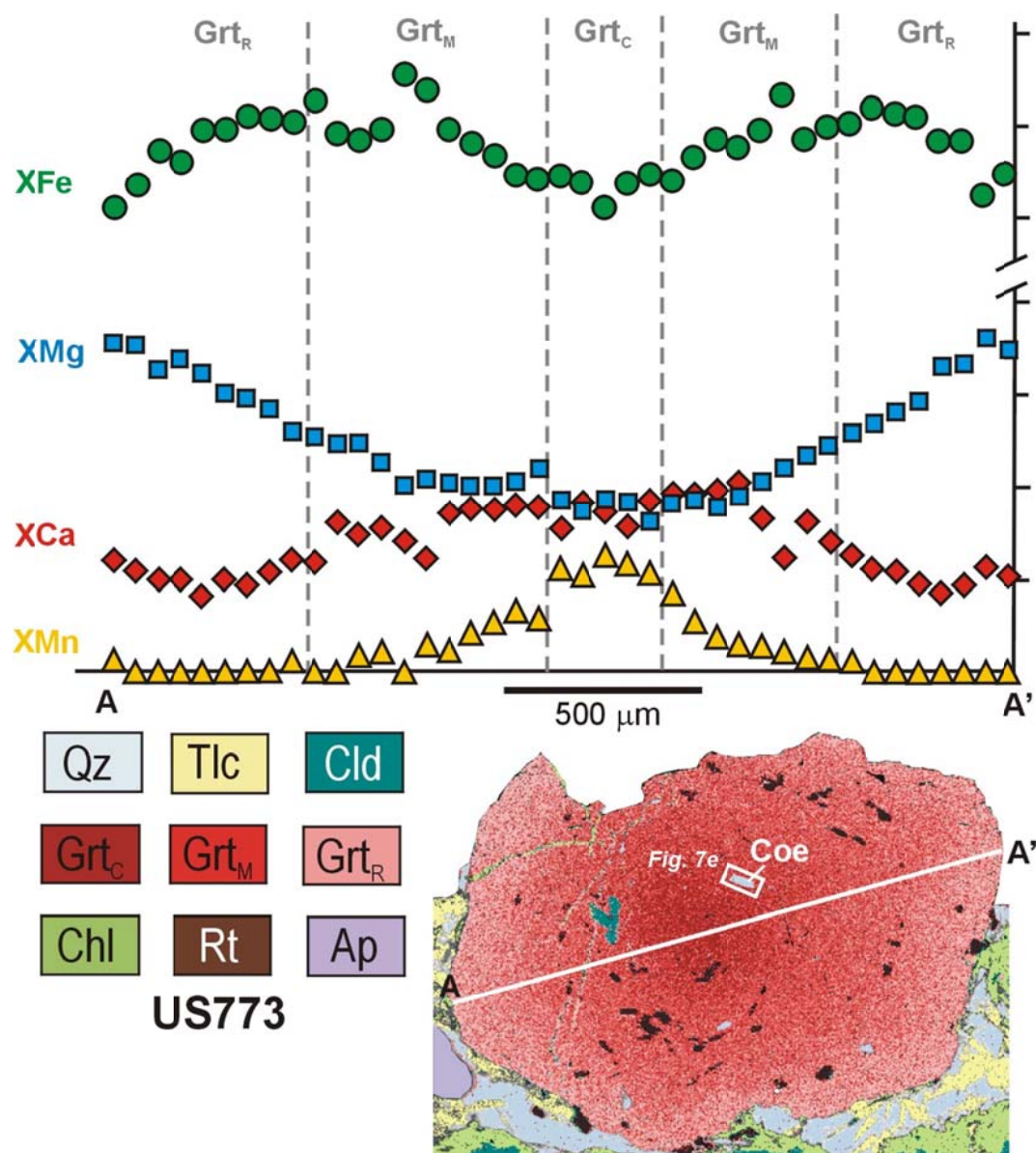


Fig. S1 - Major element chemical profile and processed X-ray map of a garnet porphyroblast from sample US773.

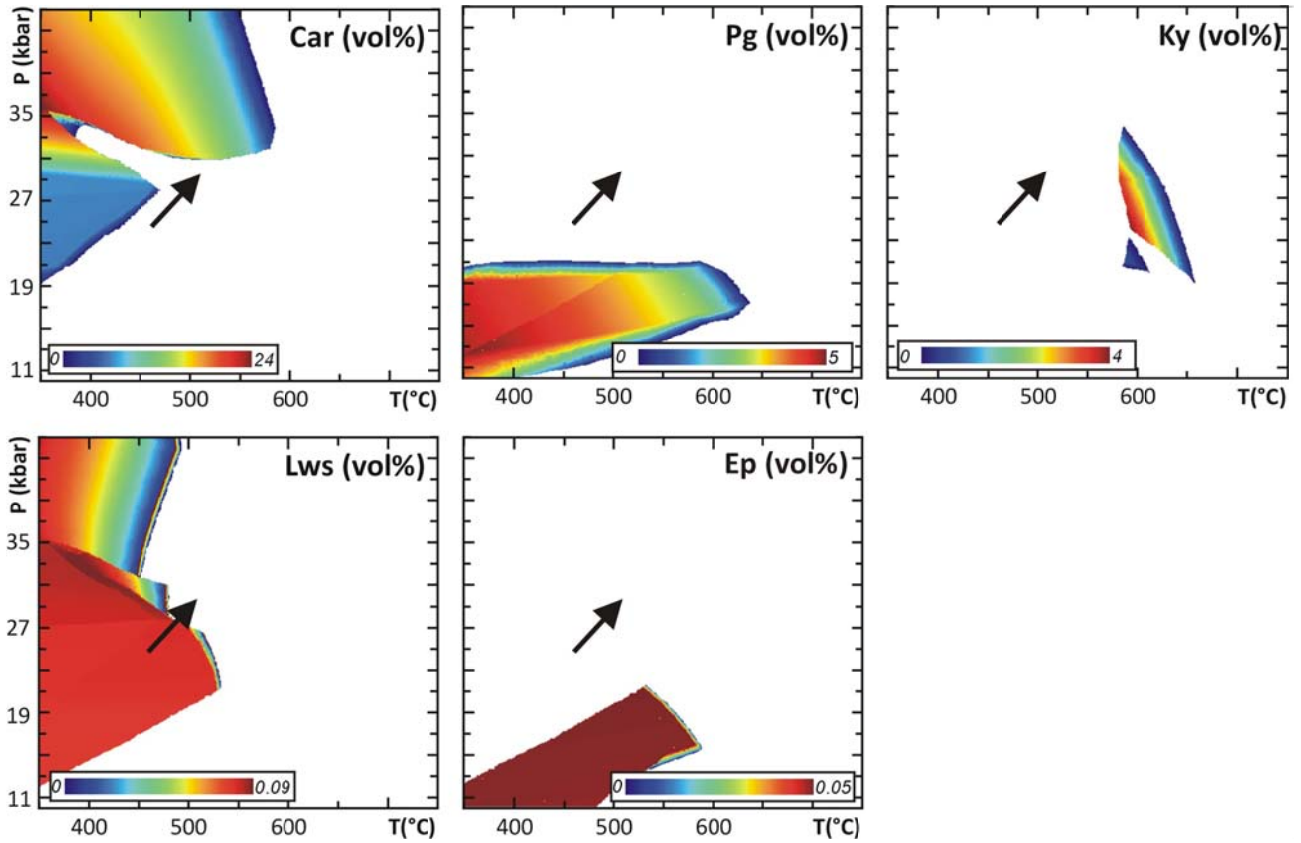


Fig. S2 - Modal variations (vol%) of mineral phases in sample US900, not reported in Fig. 8. Colours from blue to red imply higher modal proportions as indicated in each legend. The black arrow is the prograde P-T path constrained basing on the pseudosection results and YAG thermometry.

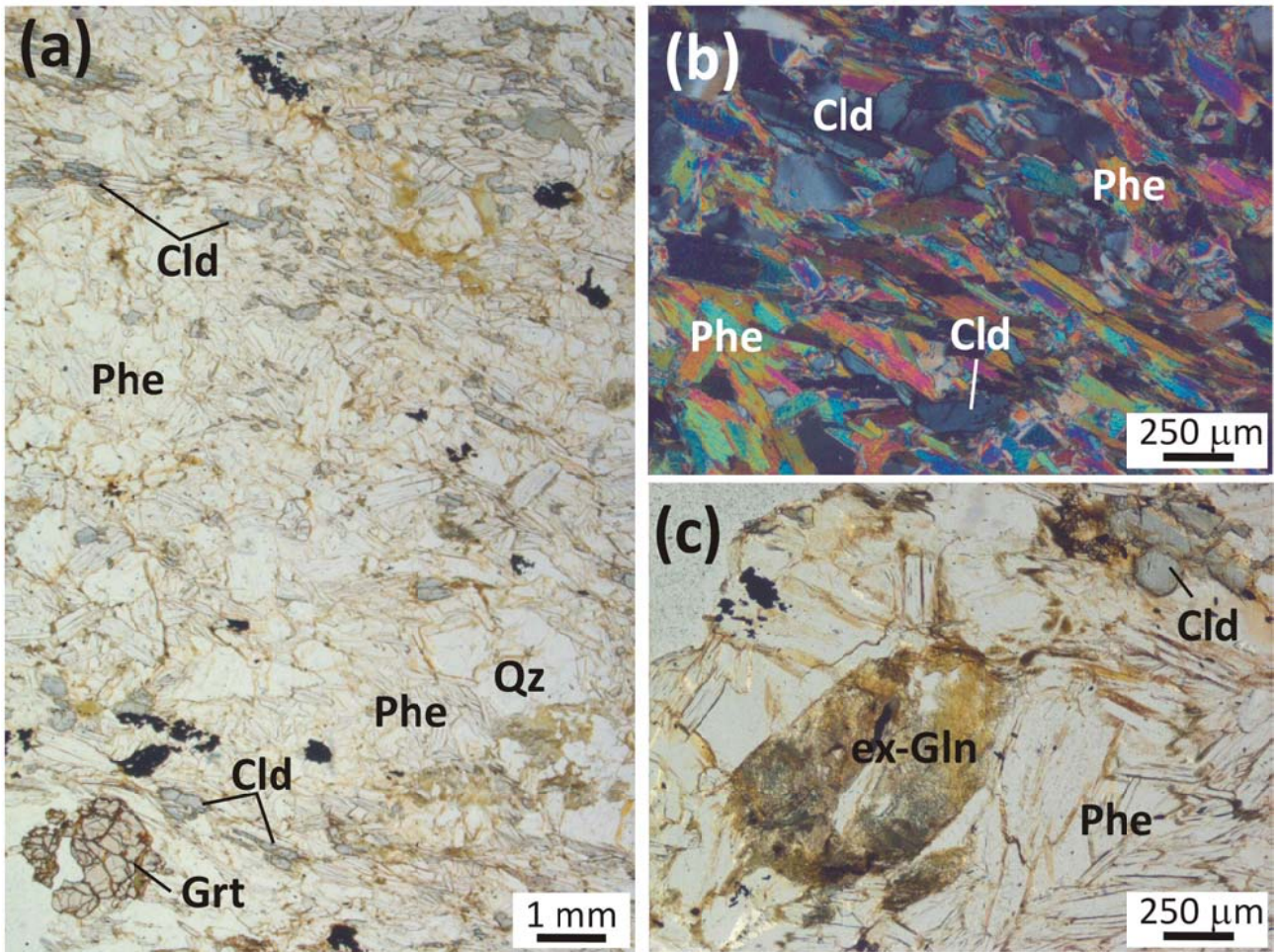


Fig. S3 - Sample LA13. (a) Representative microstructure of sample LA13 (PPL). (b) Detail of the main foliation defined by Phe and Cld (XPL). (c) Wm + Bt + Chl pseudomorph after former Gln (PPL).